CURIE POINT DEPTH MAPPING UNDERNEATH BOTSWANA FOR GEOTHERMAL PROSPECT IDENTIFICATION USING AEROMAGNETIC DATA

IZZUL QUDSI
March, 2019

SUPERVISORS:
Prof. Dr. M. (Mark) van der Meijde
Prof. Dr. F.D. (Freek) van der Meer

CURIE POINT DEPTH MAPPING UNDERNEATH BOTSWANA FOR GEOTHERMAL PROSPECT IDENTIFICATION USING AEROMAGNETIC DATA

IZZUL QUDSI
Enschede, The Netherlands, March, 2019

Thesis submitted to the Faculty of Geo-Information Science and Earth Observation of the University of Twente in partial fulfillment of the requirements for the degree of Master of Science in Geo-information Science and Earth Observation.
Specialization: Applied Earth Sciences

SUPERVISORS:
Prof. Dr. M. (Mark) van der Meijde
Prof. Dr. F.D. (Freek) van der Meer

THESIS ASSESSMENT BOARD:
Prof. Dr. N. (Norman) Kerle (Chair)
Prof. Dr. C (Christine) Thomas (External Examiner, University of Muenster, Germany)

ABSTRACT

The East African Rift System (EARS) is widely recognized as a major tectonic system that has excellent geothermal resources. A recent study in southern Africa found that there might still be rifting in the Passarge Basin in central Botswana, suggesting that the East African Rift System (EARS) is extended. This research was done to examine the implication of the extension of the EARS to the geothermal prospect that could be used as the preliminary information for further exploration in Botswana.

In this research, the Curie point depth (CPD) and heat flow map of Botswana were produced from aeromagnetic data. The method used was the spectral analysis (1DPSD) which considered as the ideal approach for a regional CPD study. This method has several parameters dependency, the p*ycurious* algorithm was applied to overcome this issue. A window size 400 km with increments of 50 km was used in the algorithm to produce the CPD deeper than 40 km (based on the crustal thickness estimated in this region). The CPD and heat flow maps were compared to the existing geophysics and geological information to examine the implication of the extension of EARS to the geothermal prospect of Botswana. The prospective zones were delineated according to the heat flow value and the geological condition.

The result indicates that the CPD appears to be consistent with the previously published crustal thickness model for the northern part of Botswana. The shallower CPD zones (<15km) are coincident with the thinner crust zones from the model (<40 km). These zones were distributed along the geologically weak area, from the northern part which is represented by the Ghanzi-Chobe Belt to the south-western part represented by the Nosop Basin. The heat flow map created was able to distinguish the high heat flow (>65 mW/m^2) area that was comparable to the heat flow value in the well-developed geothermal field in the western branch of EARS. Two prospective geothermal zones were identified based on the anomalous heat flow, divided by the possible tectonic condition that caused the anomaly. The first zone was interpreted as the result of the continuation of the EARS, the other zone was interpreted as the result of the older tectonic activity in Early Proterozoic era or the current tectonic activity as indicated by the recent earthquake in this area.

Keywords: Curie Point, Heat Flow, Aeromagnetic, Botswana, East African Rift System, Crustal Thinning, Geothermal.

ACKNOWLEDGMENTS

Firstly, I praise and thanks to Allah Almighty for the knowledge, strength and the wonderful opportunity for me to complete my MSc program in this beautiful country. I also want to thank the ITC Excellence Scholarship Program for supporting my study financially.

My most gratitude to my Supervisors, Prof. Dr. M. van der Meijde and Prof. Dr. F. van der Meer for their patience, guidance, comments and advice. Thank you for always willing to share the precious time whenever I ran into trouble or had questions. I would also thank Mr. Islam Fadel for the discussion regarding the basic geophysical knowledge during the early phase of the research. I also like to thank Chris, Harald, Wim, Frank, Caroline, Rob and all the staff in Applied Earth Science department.

To my classmates in Geological Remote Sensing and my Indonesian colleagues, thank you for the memorable stories we've shared in the past 18 months. It is not the end of the story, it is just the beginning of our friendship that will last forever.

Special thanks are due to my parents, Ir. Miftakhul Huda Aufa and Amanatullah, for their limitless support. My thanks are also extended to my siblings, Andin, Della, Abel and Rara.

To many people who have helped me in completing this thesis, I thank you all.

TABLE OF CONTENTS

LIST OF FIGURES

LIST OF TABLES

1. INTRODUCTION

1.1. Problem definition

The potential of geothermal exploration in Africa is growing along the continuation of the East Africa Rift System (EARS). This system is one of the major tectonic structures of the earth that facilitate the heat energy to escape to the surface (Rojas, 2015). EARS forms a south-western branch which consists of Quaternary rift basin from Lake Tanganyika to the Okavango Rift Zone (ORZ) at the north-western part of Botswana (Kinabo et al., 2007). However, Botswana has not been considered as a country with geothermal potential yet currently. Bertani (2017) mentions that there is no other country in Africa with geothermal power installed beside Kenya and Ethiopia. There is a company from Botswana called Kalahari Energy that is working on geothermal exploration in Zambia, instead of in Botswana (Richter, 2011). Apart from those cases, Botswana might have a geothermal reservoir in the ORZ according to the regional study of deep aquifer temperature by Limberger et al. (2018). There is an area in Botswana has high aquifer temperature that reaches approximately 100^0C referring to this paper, however many of the area in Botswana was not calculated due to the sediment thickness beyond the cut off they used.

A recent study in southern Africa found that the initiation of rifting occurs at Passarge Basin in central Botswana, suggesting that the EARS system is not ended at ORZ but extended to the border of Congo Craton in the west and Kaapvaal Craton in the south (Fadel, 2018). According to this fact, it is interesting to study the implication of this new theory to the geothermal resources in Botswana. The result might discover the bigger geothermal prospect underneath Botswana, compared to the current knowledge.

Rift system zones are considered as the most attractive tectonic setting for blind geothermal system identification (King, Metcalfe, Fellow, Office, & Office, 2013). The amount of magma supply in the rifting zones will significantly increase the heat flow and thermal energy at shallower depth. The shallower the depth, the higher the potential of the existence of high temperature at the near surface. This phenomenon could provide heat for the reservoir of the geothermal system. The further geological and geophysical study is necessary to understand the impact of the continuation of EARS on the geothermal prospect of the study area.

Nowadays, various geophysical studies have been performed in Botswana and published where some of them created the crustal and upper mantle models. The most recent study was done by Fadel (2018) using the NARS-Botswana seismological dataset combined with four other seismological networks reveals that the very low velocity in the southern part of Botswana as the signature of crustal thinning activity. Research on magnetotelluric (MT) was performed recently in the entire Botswana and southern Africa. The research states that a localized deep-seated high conductivity anomaly as the typical rift signature of a thinned lithosphere does not exist at the ORZ (Khoza et al., 2013). Therefore, it is in contrast with the previous studies by Chapman & Pollack (1977) and de Beer et al. (1976), which suggest that there is an anomalous conductivity at this zone and this anomaly conductivity is partly originated from thermal due to the rifting process.

A geophysical study on Curie-point Depth (CPD) needs to be done to define a geothermal prospect in Botswana. CPD is the depth at which temperature reaches the value of the Curie point of magnetite at ~851^0 K (Eppelbaum, Kutasov, & Pilchin, 2014). The lifted heat from the earth crust could potentially be the heat source of a geothermal reservoir. The Curie point depth could indicate the area with the high possibility of magma upwelling that caused the higher temperature to appear in a shallower depth. CPD could also be a sign of a crustal thinning activity based on this information.

CPD mapping using the latest method by Bouligand et al. (2009) was implemented in Australia by Chopping & Kennett (2015). They used a novel procedure to extract the spatial wavenumber representation for the required one-dimensional power spectra to stabilize the longest wavelength components of the magnetic anomaly dataset. This approach was performed not only to stabilize the average spectrum, but also to produce the standard deviation of the result that represents the spatial noise. CPD map could be used to calculate the heat flow to understand the subsurface thermal structure of the study area.

Research about CPD in the northern part of Botswana was performed by Leseane et al. (2015) using 3-D inversion method. The result discovers the zones with shallow Curie-point values (8-15 km) and high heat flow (60-90 mW m^{-2}). Heat flow values from the result are similar to the heat flow reported earlier by Ballard, Pollack, & Skinner, (1987). This result is also comparable with the value from the Kivu, Tanganyika and Malawi rifts in the western branch of EARS. The spatial distribution of the shallow zones is coincident with the continuation of EARS in Botswana.

However, the study by (Leseane et al., 2015) is covering only a small part of Botswana. Furthermore, the method used is considered less accurate for regional CPD estimation study and will only effective for small scale research. Another method needs to be performed to overcome this obstacle. Accordingly, the CPD estimation using the power spectrum was applied in this research to map the CPD of entire Botswana. This method selected in order to deal with the bigger area and the CPD that theoretically deeper especially in the Cratonic zone.

This study will produce the missing geophysical analysis, Curie-point depth and heat flow map of the study area using aeromagnetic data. The results will be compared to the previously-published crustal thickness model and the basement geology to analyse the subsurface thermal variation of the study area. This information will be used to assess the relationship between shallow curie-point depth area and crustal thinning theory and its implication to the geothermal prospect in Botswana

1.2. Research objectives

The main objective of this research is to discover the geothermal prospect in Botswana by integrating Curie depth and heat flow map with the previous subsurface information such as crustal thickness, Moho depth model and the basement geology map.

- Research objectives:

1. To evaluate the relationship between CPD map and the crustal thinning theory in the study area.
2. To analyse the heat flow value and the spatial distribution in the study area.
3. To indicate the geothermal prospect of the study area.

1.3. Research questions

- Research questions:

1. Which area has shallow CPD? What is the value of the shallowest CPD?

2. How is the spatial relationship between the shallow CPD area and the observed crustal thinning in the study area?
3. How is the heat flow value of the study area compared to the value of the developed geothermal field in the EARS? What is the effect of the different basement geology on the heat flow value?
4. What is the implication of the crustal thinning theory to the geothermal prospect of the study area?

1.4. Thesis structure

This thesis constructed by 6 chapters which summarized below:

Chapter 1: Introduction

Explains the definition of the problems, the research objectives and research questions.

Chapter 2: Study Area

Consist of the information regarding the location of the study, geological and geophysical condition of the study area. This chapter also provides information from the developed geothermal field near the study area.

Chapter 3: Dataset

The description of the dataset used in this research.

Chapter 4: Methods

The description of how the dataset used include the consideration regarding the method and parameter selection that was used in this research.

Chapter 5: Results and discussion

This chapter describes the results of the Curie point depth and the heat flow estimation includes the discussion of the result and comparison with the previous model and information available.

Chapter 6: Conclusion and recommendations

This chapter includes the conclusion and recommendation for further research.

2. STUDY AREA

The study area of this research is the entire country of Botswana, located in the southern part of Africa. Topographically, Botswana is a flat terrain country with most of the territory being covered by the Kalahari Desert. This country bordered by South Africa in the south and east, Namibia in the north and west and Zimbabwe in the northeast.

2.1. Tectonic and geology of the study area

Geologically, the study area is part of the Precambrian crust of Africa which consists of Proterozoic orogenic and Archean rocks. Summarized from several references (Chisenga, 2015; Fadel, 2018; Key & Ayres, 2000; Singletary et al., 2003), Botswana is consist of two Cratonic blocks, Kalahari and Congo Craton. The oldest rocks exposed in Botswana come from the Archean terranes of Kalahari craton; Kaapvaal and Zimbabwe cratons and the Limpopo Mobile Belt.

The younger Proterozoic rocks such as Magondi and Kheis Belts are mostly concealed underneath the Karoo rocks in the western side of the Kalahari Craton. These rocks are poorly exposed in the surface but clearly identified by regional magnetic maps. Ghanzi-Chobe belt started to develop also in the Proterozoic era due to extensional forces as the consequence of the Kibaran Orogeny collision event along the Namaqua-Natal belt in South Africa. Reactivation of Kheis province and the amalgamation of the Rehoboth province also happened during this period. The youngest tectonic event before the infamous East African Rift System was the formation of the Damara-Ghanzi Cobe belt and the formation of Passarge and Nosop sedimentary basins from Neoproterozoic to early Paleozoic. The East African Rift System itself began to develop from the Cenozoic era in the Miocene period.

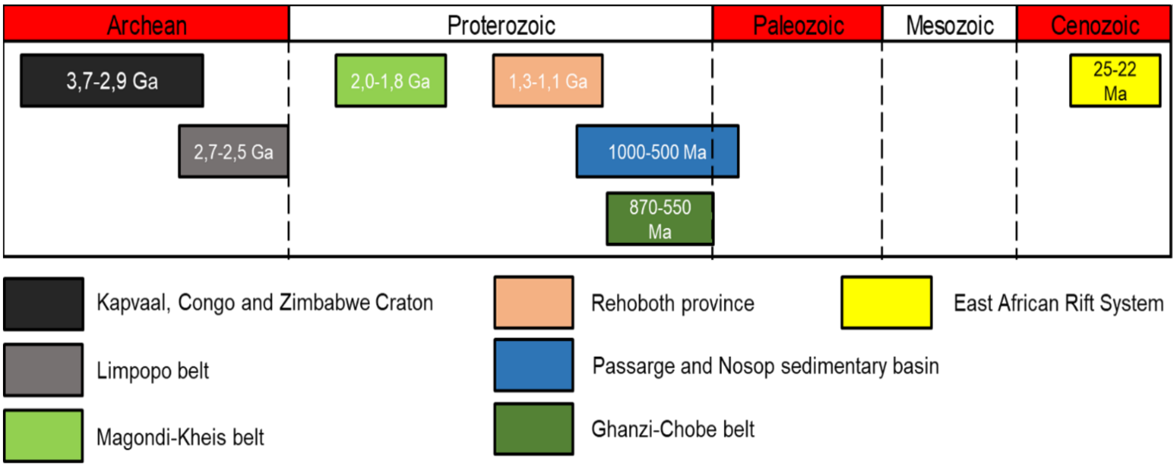

Figure 1 The tectonic events in Botswana modified from Fadel, (2018)

Kinabo et al. (2007) explain that the part of EARS also appears in Botswana. The south-western branch of EARS is extended to the north-western part of Botswana at ORZ (Omenda, 2013). Recently, Fadel (2018) reveals that the continuation of this branch of EARS is also extended until the border of Kalahari and Congo cratons in the southern part of Botswana, according to the result from the seismological study. The seismic activities of the study area indicate that the very low shear wave velocity as the signature of crustal thinning is not just ended in ORZ.

The most recent basement geology was mapped by Chisenga, (2015) using gravity and magnetic data. The author added two important things in the updated basement geology map of Botswana, the tectonic boundary and terrain which express the directional forces of the tectonic activity and the mafic intrusion that indicate the activity of the crust due to the movement of the magma from mantle to surface as the result of extension or rifting (Figure 2).

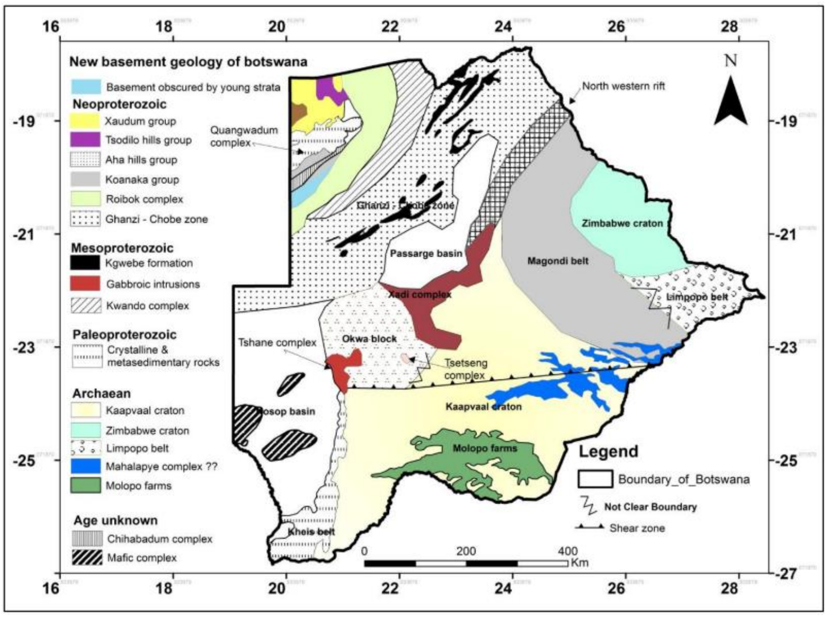

Figure 2 Updated basement geology map using gravity and magnetic data (Chisenga, 2015)

2.2. Geophysical studies in Botswana

Several geophysical studies were performed to analyse the subsurface configuration of the study area. The most recent study was done by Fadel (2018), that models the crustal thickness using the compilation of several seismological networks across Botswana (NARS, SASE and SAFARI). The result of the Vp/Vs ratio and crustal thickness for entire Botswana are showing that there is a crustal thinning activity in the Central and Southwestern part of the study area (Figure 3a and 3b).

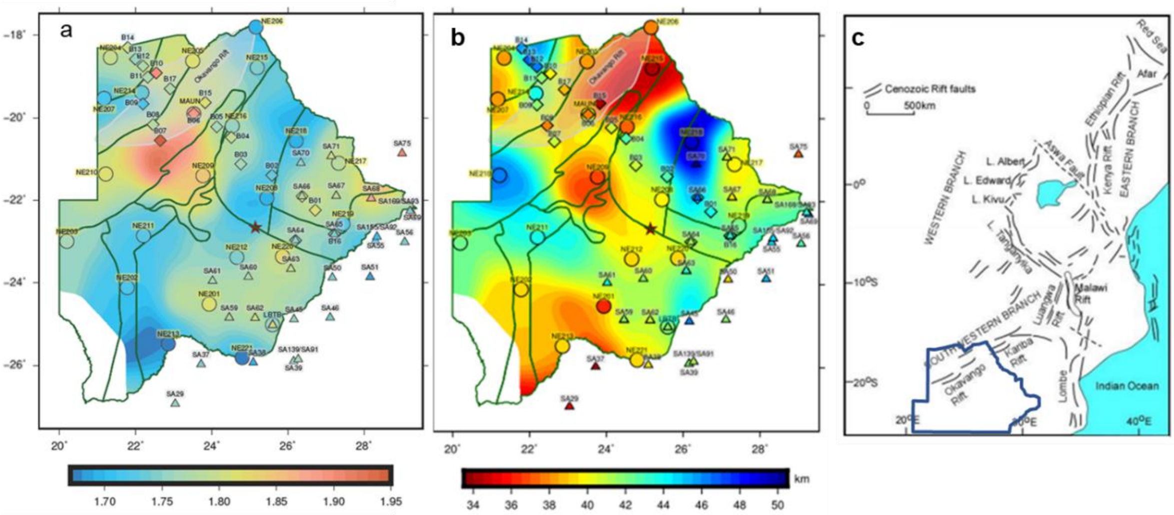

Figure 3 a) VP/VS ratio and b) crustal thickness model by Fadel (2018). c) The structural map is showing that the continuation of the south-western branch of EARS is ended at Okavango Rift (Omenda, 2013). The circle, triangle and square on the VP/VS and crustal

The crustal thinning theory proposed by the author is triggering the idea of this study to investigate further regarding the Curie depth and its relationship with the geothermal prospect of this area.

Another geophysical study was done by Chisenga, (2015) that produces a Moho depth model using gravity and magnetic data analysis (Figure 4). The distribution of the shallow Moho depth at this model is consistent with crustal thickness model from (Fadel, 2018). The range of Moho depth in Botswana is approximately from 33-45km. This model is also showing the shallower Moho in the south-western part of Botswana that related to the sedimentary basin which might be influenced by the old rift activity in this area. This model used as the comparison of the depth of Curie point estimated by this research.

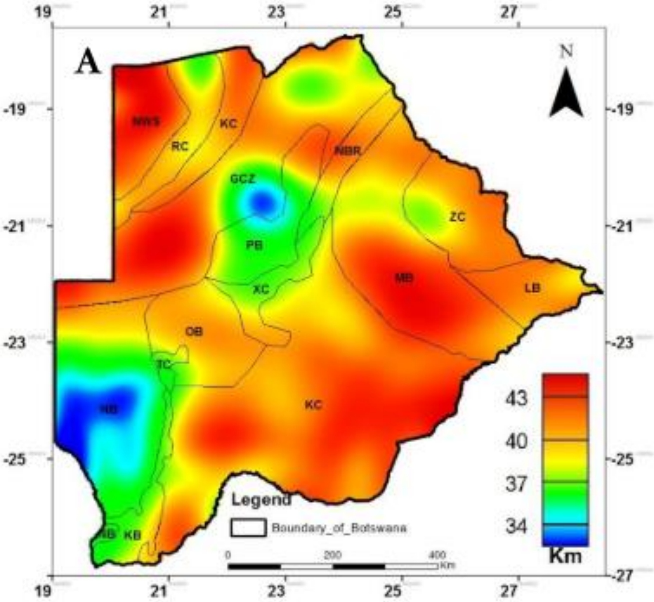

Figure 4 Moho depth produces from magnetic and gravity data overlaid by basement tectonic map (Chisenga., 2015)

2.3. Previous CPD study in Okavango Rift Zone (ORZ)

There was a study that estimates the CPD in the study area. Leseane et al., (2015) studied about thermal perturbation of the Okavango Rift Zone in the north-western part of Botswana. The author used the 3-D inversion of aeromagnetic data to calculate the CPD (Figure 5). According to the study result, the shallow CPD values are around 8-15km with high heat flow around 60-90 mW/m^2. The trend of these zones is coincident with the major rift that exists in the ORZ and corresponds to the thinner crust.

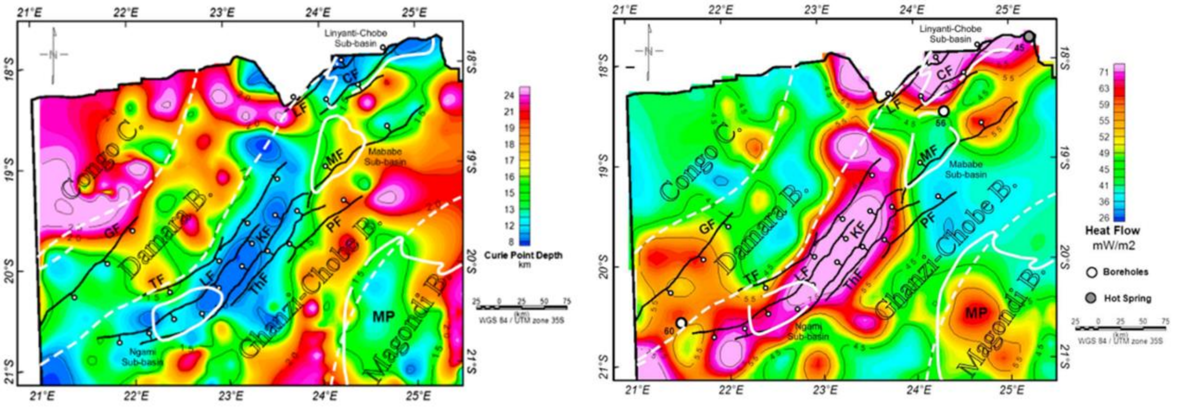

Figure 5 The left image is the Curie point depth map and the right image is the heat flow map created using 3-D inversion method by Leseane et al., (2015)

2.4. The geothermal field in East African Rift System

The East African Rift System (EARS) is the series of valley that extended for more than 4000km from Afar triangle to Mozambique (Omenda, 2013). The central part of EARS is referred to the Kenya dome (volcanic zones) that stretch and fracture the outer crust into host and graben structures associated with a normal fault, the typical feature of a rift valley. According to King & Metcalfe, (2013), geothermal fields in EARS are characterized by shallow heat source approximately 6 Km and high temperatures around 300^0 Celsius. This system is categorized into two branches, the Eastern and the Western branch. There are two types of the hydrothermal system developed in this area, namely steaming ground and advective (Hochstein, 1999).

Until today, the western branch of EARS has always underestimated when it comes to geothermal exploration. However, several geothermal manifestations such as hot springs and fumaroles were found in the Tanganyika-Rukwa, Malawi rift, Zambia and Mozambique (Hardarson, 2016). Omenda, (2013) explained that these areas are also tectonically and magmatically active according to the high seismicity recorded. Geothermal surface exploration was done by a Swedish consulting group in this region between 1976 and 1976. There was also geothermal pilot plant installed in this area, the Italian government install the plant in the Lake Tanganyika but never became an operational plant.

2.5. Heat flow in East African Rift System

The heat flow in EARS has been compiled by Fadaie & Ranalli, (1990) from several studies in this area. Different heat flow values were recorded in a different part of the EARS. The average surface heat flow in Eastern Rift is approximately 106 ± 47 mW/m^2. Generally, the heat flow in the Western Rift is less than the Eastern Rift.

As explained in the previous section, the study area is part of the western branch of EARS. According to the paper, the heat flow values in this branch are; Lake Kivu (82±78 mW/m^2), Lake Tanganyika (65±36 mW/m^2) and the whole of Lake Malawi (67±46 mW/m^2). Figure 6 shows the heat flow in the western branch of EARS.

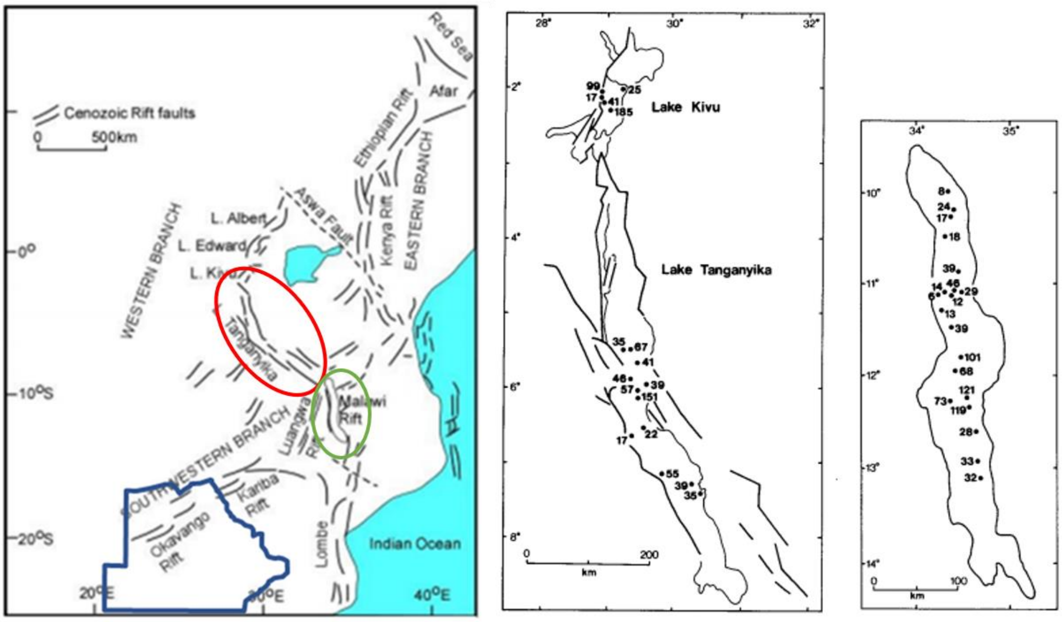

Figure 6 heat flow values at the western branch of EARS in mW/mw^2 from Fadaie & Ranalli, (1990*).* Left) Location of Lake Tanganyika indicated by the red circle and Malawi Rift indicated by the green circle. Centre) heat flow at Lake Tanganyika and Lake Kivu. Right) heat flow at Malawi Rift

3. DATASET

3.1. Aeromagnetic data

The aeromagnetic data used in this study was compiled from several aeromagnetic surveys acquired by Geological Survey of Botswana (1975-2003). The dataset already provided as a mosaic from several data and gridded at 50m pixel size (Figure 7). The coordinate system used was the Geodetic Reference System of 1980 (GRS 1980) and projected to BNGRS02 PCS COLLINS.

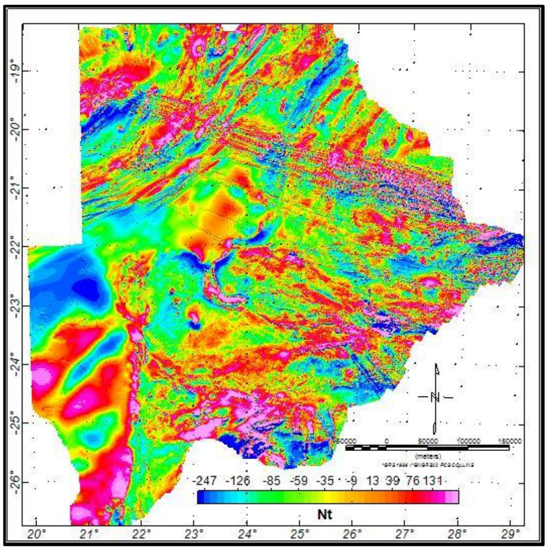

Figure 7 Aeromagnetic data of Botswana

3.2. Drill hole information

The drill hole information was used for the comparison of the CPD result and as the thermal conductivity input for the heat flow calculation and for the validation. As much as 14 wellbores were drilled over Botswana (see the distribution of the wellbore on appendix 1). This information collected from Ballard, Pollack, & Skinner, (1987). The authors provide the new terrestrial heat flow from Botswana and Namibia (table 1).

Table 1 Drill hole information across Botswana and its surrounding (Ballard et al., 1987).

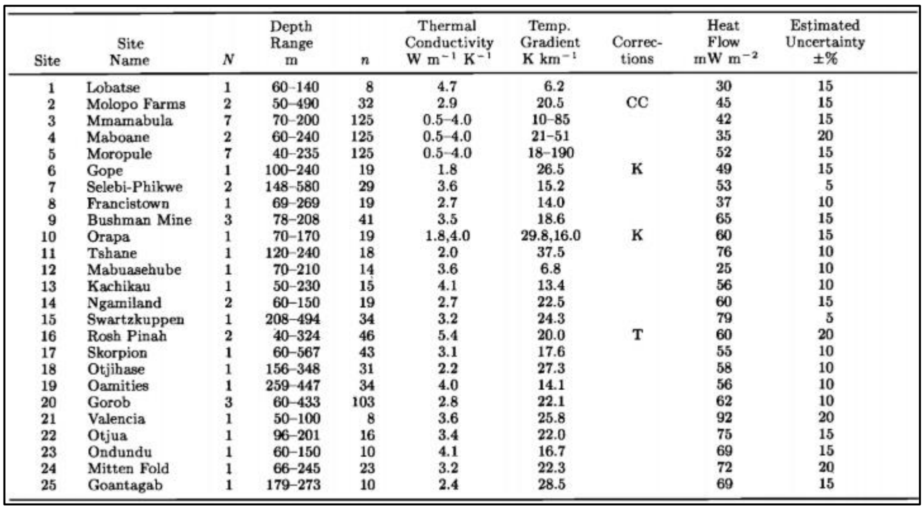

Site	Site Name	*N*	Depth Range m	*n*	Thermal Conductivity W m^{-1} K^{-1}	Temp. Gradient K km^{-1}	Corrections	Heat Flow mW m^{-2}	Estimated Uncertainty ±%
1	Lobatse	1	60–140	8	4.7	6.2		30	15
2	Molopo Farms	2	50–490	32	2.9	20.5	CC	45	15
3	Mmamabula	7	70–200	125	0.5–4.0	10–85		42	15
4	Maboane	2	60–240	125	0.5–4.0	21–51		35	20
5	Moropule	7	40–235	125	0.5–4.0	18–190		52	15
6	Gope	1	100–240	19	1.8	26.5	K	49	15
7	Selebi-Phikwe	2	148–580	29	3.6	15.2		53	5
8	Francistown	1	69–269	19	2.7	14.0		37	10
9	Bushman Mine	3	78–208	41	3.5	18.6		65	15
10	Orapa	1	70–170	19	1.8,4.0	29.8,16.0	K	60	15
11	Tshane	1	120–240	18	2.0	37.5		76	10
12	Mabuasehube	1	70–210	14	3.6	6.8		25	10
13	Kachikau	1	50–230	15	4.1	13.4		56	10
14	Ngamiland	2	60–150	19	2.7	22.5		60	15
15	Swartzkuppen	1	208–494	34	3.2	24.3		79	5
16	Rosh Pinah	2	40–324	46	5.4	20.0	T	60	20
17	Skorpion	1	60–567	43	3.1	17.6		55	10
18	Otjihase	1	156–348	31	2.2	27.3		58	10
19	Oamities	1	259–447	34	4.0	14.1		56	10
20	Gorob	3	60–433	103	2.8	22.1		62	10
21	Valencia	1	50–100	8	3.6	25.8		92	20
22	Otjua	1	96–201	16	3.4	22.0		75	15
23	Ondundu	1	60–150	10	4.1	16.7		69	15
24	Mitten Fold	1	66–245	23	3.2	22.3		72	20
25	Goantagab	1	179–273	10	2.4	28.5		69	15

3.3. Geology map

There were two geology maps used in this study. The basement geology by Chisenga, (2015) and bedrock geological map from Botswana Geoscience Portal by Geosoft. The first map contains information of the tectonic provinces and the regional structures, the second has more detailed information such as the rock type, formation, group, etc.

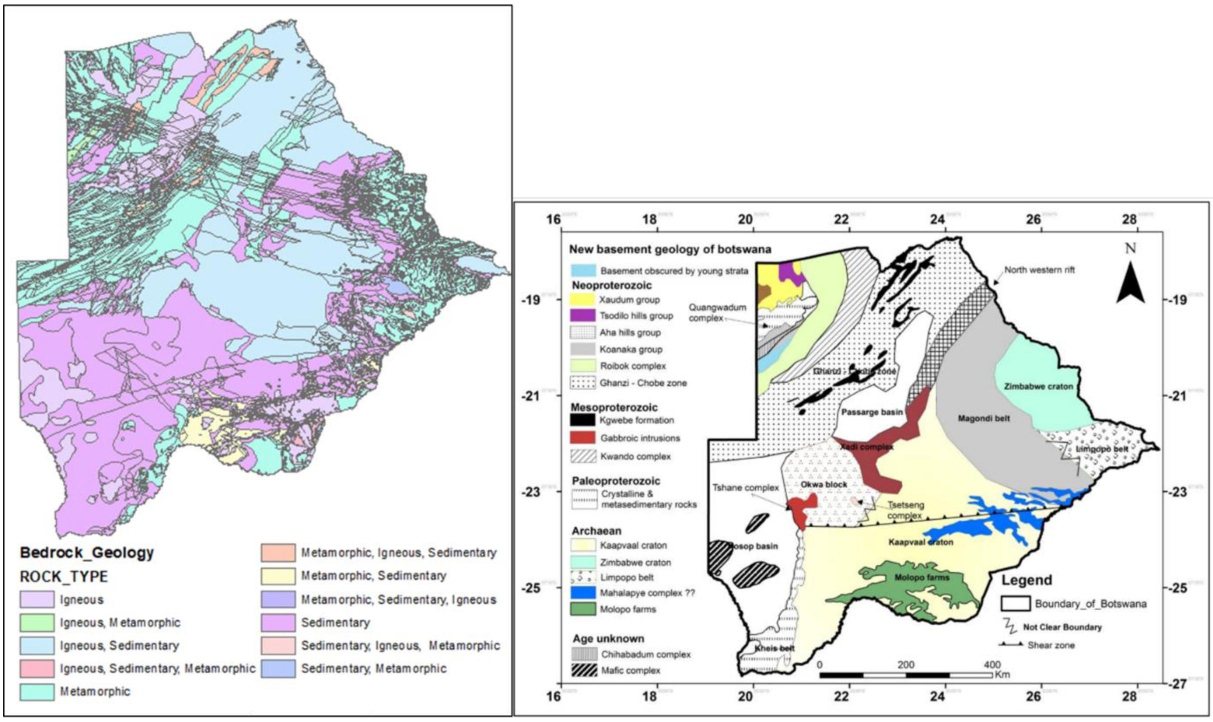

Figure 8 Left) Bedrock geology map from Botswana Geoscience Portal by Geosoft. Right) Basement geology map from Chisenga, (2015).

4. METHODS

This section describes the methods that were used in the calculation of CPD and the heat flow in this study as summarized in figure 9 below.

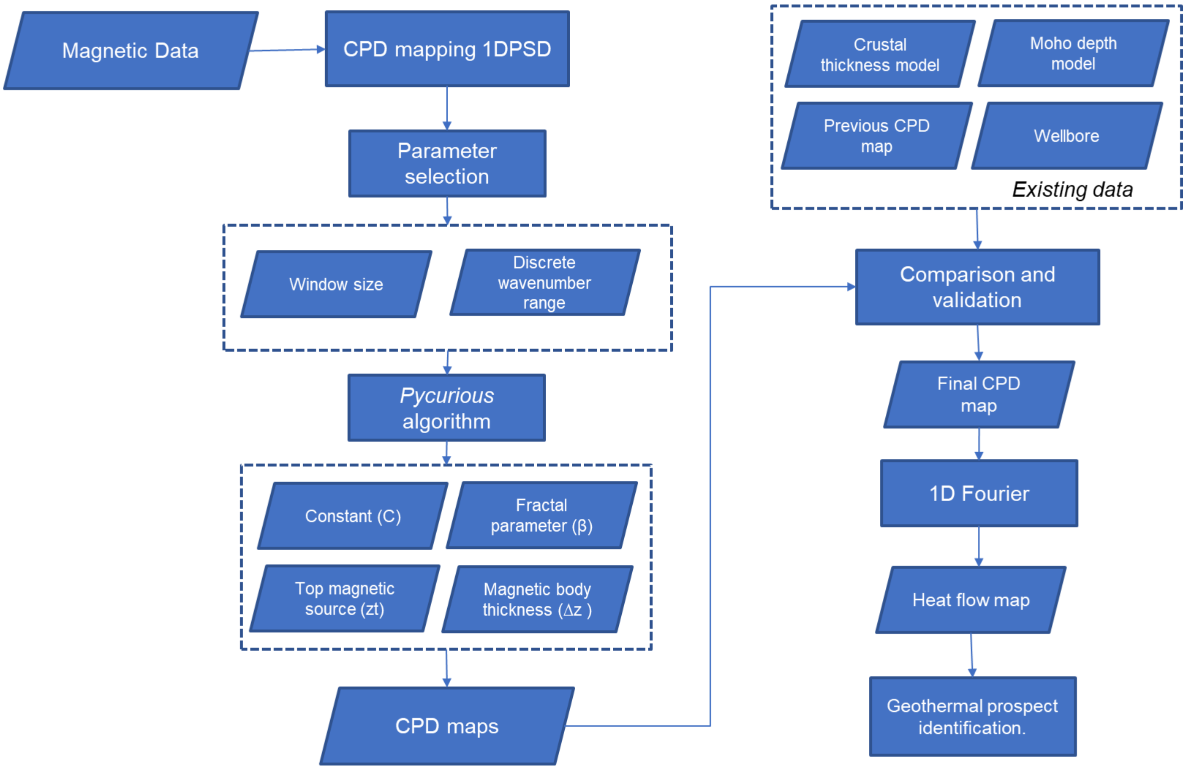

Figure 9 Research methodology flow chart

4.1. Curie depth mapping

There are several methods available to calculate the CPD of an area. In this research, CPD map was generated by deriving the depth of the bottom of the magnetic body to the surface using spectral analysis from aeromagnetic data. This method was selected to map the CPD variation on a regional scale, especially to reach the deeper CPD of the cratonic zones in the case of this research. However, this method has a limitation in mapping the shallower CPD and only provides the relative depth variation, not the actual CPD value (Bouligand et al., 2009).

The cratonic zones are expected to have a very deep CPD, which the spectral analysis is the ideal method to deal with this issue. The heat flow information retrieved from wellbore data and the CPD model from 3-D inversion of magnetic data by Leseane et al. (2015) at the Okavango zone were used as the comparison of the CPD estimation from the aeromagnetic data in this study.

4.1.1. Depth estimation from spectral analysis

There are several methods and variations have been proposed in estimating the depth of the magnetic feature from averaged Fourier spectra. This method was originally introduced by Spector & Grant (1970); they estimate the depth of the source from the slope of the plot between the log of power spectrum versus wavenumber (Figure 10). Many authors later use and develop the method for further study purposes, Maus et al., (1997) estimate the Curie-temperature depth based on this method with the fractal parameter consideration.

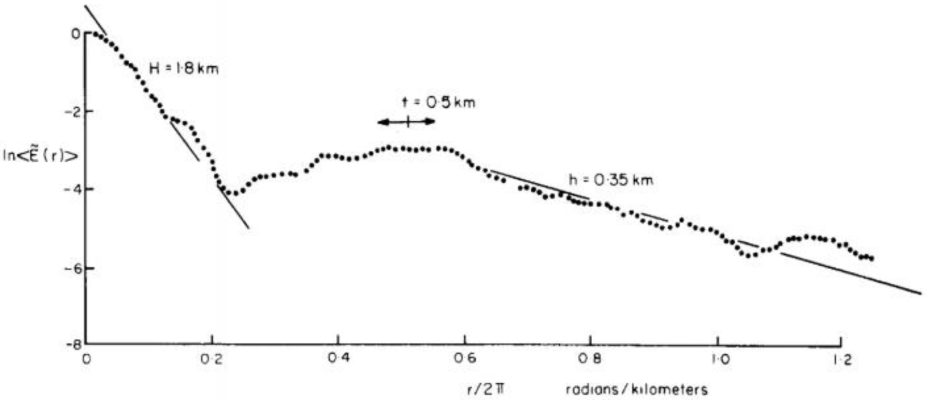

Figure 10 Power spectrum analysis of an aeromagnetic map and the depth estimation by Spector and Grant (1970). H = the depth of the source. If there is more than one slope, the slope at smaller wavenumber gives the depth of the deeper sources.

In this study, the CPD map was generated using the 1-D Power Spectra Density (1DPSD) method (equation 1) developed by Bouligand et al., (2009) from the aeromagnetic data. This method creates the fractal model for crustal magnetization instead of using self-similar value as proposed by Maus et al., (1997).

$$\begin{aligned}\Phi_{B1D}(k_H) = {} & C - 2k_H z_t - (\beta - 1)\ln(k_H) \\ & + \left[-k_H\Delta z + \ln\left(\frac{\sqrt{\pi}}{\Gamma\left(1+\frac{\beta}{2}\right)}\left(\frac{\cosh(k_H\Delta z)}{2}\Gamma\left(\frac{1+\beta}{2}\right)\right.\right.\right. \\ & \left.\left.\left. - K_{\frac{1+\beta}{2}}(k_H\Delta z)\left(\frac{k_H\Delta z}{2}\right)^{\frac{1+\beta}{2}}\right)\right)\right] \end{aligned} \qquad (1)$$

where kH is the wavenumber, zt is the top of a magnetic source, Δz is the thickness of magnetic sources, β is the fractal parameter and C is a constant.

This method very much depends on four parameters (C, β, zt and Δz), it needs to be defined. Selecting the wrong parameter will lead to the wrong power spectrum calculation result. Instead of manually simulate each of the parameters, a python module called *pycurious* was used to avoid the dependency of the CPD result with the parameter selection. This module seeks the 1DPSD parameters using Maximum a Posteriori (MAP) algorithm with the searching increments 0.25 for the β, 0.1 for the zt, 1.0 for the Δt and 0.5 for the C from thousands of simulations. Curie point depth value generated from the mean of zt + the mean of Δz. The uncertainty of the result is the standard deviation of zt + Δt.

The author of the *pycurious* algorithm suggests that prior constraints need to be applied to tackle the problem of unrealistic depth result. In this study, the depth of Moho and crustal thickness information was added as the depth constraints over the CPD from 3-D inversion. Apart from the reason that these models are covering entire Botswana, the result of 3-D inversion tends to underestimate the depth of the CPD that makes this model is less accurate especially in the deeper CPD such as in the Cratonic zone.

This algorithm was applied to the discrete wavenumber (different method was used in this study for selecting the discrete wavenumber) of the aeromagnetic data with a moving window over entire Botswana using various sizes with an increment of 50 km. This algorithm requires a square dataset, while the extent of aeromagnetic data provided was limited to the boundary of Botswana. A taper was applied to the dataset to generate the interpolated magnetic value outside the boundary.

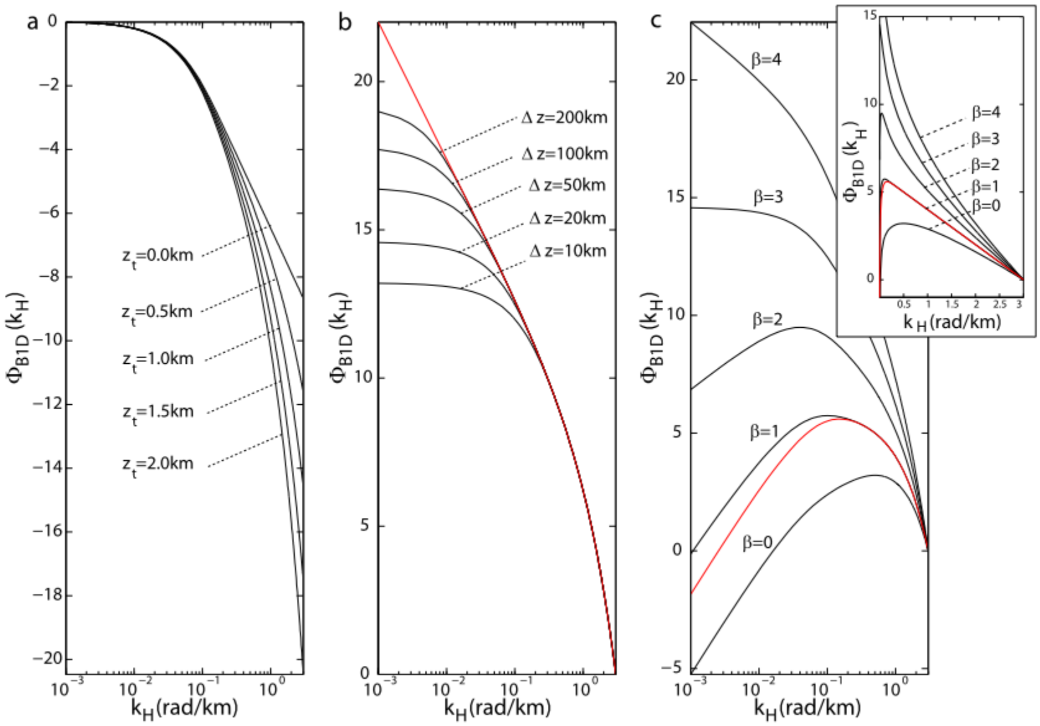

Figure 11 Theoretical radial spectra of magnetic anomaly predicted for different values. Values of two other fixed parameters are zt=1km, Δz =20km and β = 3. The red curve is the theoretical radial power spectrum used by earlier studies where the C values are constant (Bouligand et al., 2009)

According to theoretical radial spectra of magnetic data (Figure 11), the divergence of Δz occurs at the lower wavenumbers as the layer thickness increases. This low wave numbers will be the range that gives information of the bottom of the magnetic sources. The bigger window size was applied in order to discover the deeper magnetic sources to settle with this issue.

4.1.2. Discrete wavenumber selection

Before applying the *pycurious* algorithm, the high-resolution aeromagnetic data were resampled. Not only to make the data into a manageable proportion but also to select the wavenumber range of the data used in the CPD calculation. The very high wavenumber influenced by the small features around 50m (original pixel size) is not necessary to be included in mapping a depth with the size of around kilometers deep, these features will affect the smoothness of the spectrum calculation. The resampling operation will give a smoother spectrum and consequently remove the higher wave number of the dataset. This wavenumber range from the resampled images was used to calculate the 1DPSD.

In this research, the resampling method used was adapted from (Chopping & Kennett, 2015), the aeromagnetic data were resampled and averaged in the frequency domain. This approach selected in order to retain the spatial component with higher fidelity as compared to the simple resampling method.

The aeromagnetic data were resampled into three different pixel size; 200m (4-fold reduction), 400m (8-fold reduction) and 800m (16-fold reduction). In this resampling method, every pixel from the original image was taken to represent the coarser pixels in the resampling image by taking the sampling pixels 1 by 1 per 4x4, 8x8 and 16x16 of the dataset. This resampling operation produces 16, 64 and 256 realizations which then transformed and averaged using Fast Fourier Transformation (FFT). Fourier transformation converts the signal from its original domain to a representation in the frequency domain. In this process, the data were converted from a spatial domain. The last step was inverting back each result into a spatial domain to be processed for the CPD calculation. Figure 12 shows the process of the aeromagnetic data resampling.

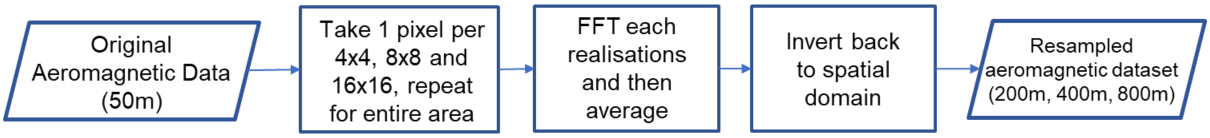

Figure 12 Aeromagnetic data resampling process.

4.1.3. Window size selection

As mentioned earlier, the window size selection needs to be determined based on the depth of the magnetic source that needs to be covered. While the resampling operation has influence in the higher wavenumber range, the window size selection influences the lower wavenumber range. This is a very crucial factor in the CPD calculation using the power spectrum method as the Δz mainly related to this wavenumber range.

Several window sizes were applied in order to investigate the influence of the sizes as the consideration in selecting the size used in this study. The *pycurious* algorithm then applied to the three resampled data with various window size to select the correct window size.

The rule of thumb of the window selection is to use the window size tenth times of the deepest CPD expected (Bouligand et al., 2009). Several window sizes from 350km to 650km increasing by 50km were applied to each dataset at the central part of the study area to cover the depth of magnetic source around 35-65km (Figure 13).

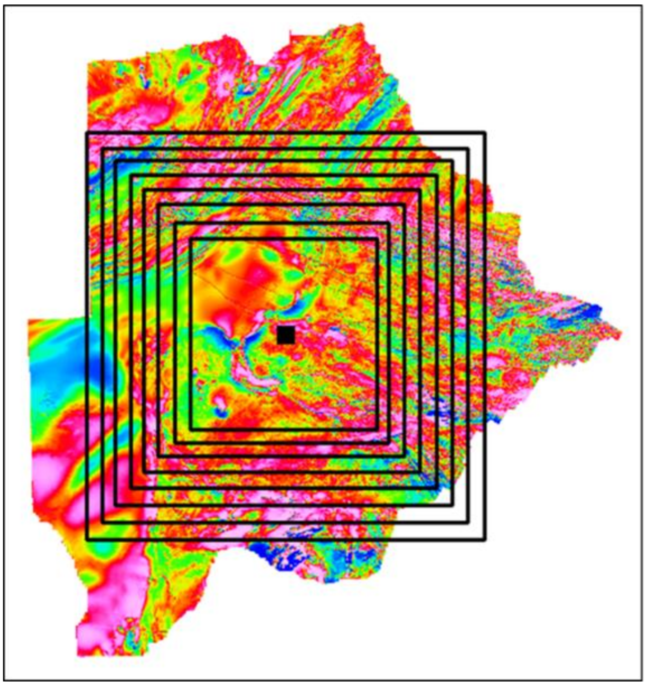

Figure 13 Different window size applied to the dataset from 350km as the smallest window size increasing 50km to the 650km as the biggest window size.

4.2. Heat flow calculation

The heat flow (q) estimated using 1-D Fourier's Law equation from the CPD map;

$$q = k\ (dT/dz) \tag{1}$$

where k is thermal conductivity and (dT/dz) is the temperature gradient. The k value will be taken from the thermal properties of each lithology in different tectonic provinces in Botswana measured by Ballard et al., (1987).

According to Tanaka et al. (1999), Curie temperature (C) is defined as temperature gradient multiplied by the depth (D).

$$C = (dT/dz)\ D \tag{2}$$

As suggested by MT data (Khoza et al., 2013), there is no other heat source (conductivity anomaly) between the CPD and the surface. Then the equation for heat flow could be simplified as;

$$D = k\ C/q \tag{3}$$

Heat flow calculation from the wellbore in Botswana by Ballard et al., (1987) was used to validate the calculation result of this study. The result also compared to the heat flow of the developed geothermal fields in EARS specifically in Kenya and Ethiopia, to define the area with a geothermal prospect.

Different thermal conductivity values were assigned to different tectonic provinces to calculate the heat flow of the study area. The value assignment is based on the dominant rock that presents in each province. Cermak & Rybach, (1982) published the value of thermal conductivity of each rock (appendix 2). The value range of thermal conductivity provided by the paper is in a quite large range, this makes the values were often considered as questionable. A recent publication by Mielke, Bär, & Sass, (2017) discussed the correlation of thermal conductivity of each rock with compressional wave velocity and porosity and gave a more detailed thermal conductivity value with a standard deviation smaller than 0.5 W/m K (table 2).

Table 2 Thermal conductivity of common rocks after Mielke et al., (2017)

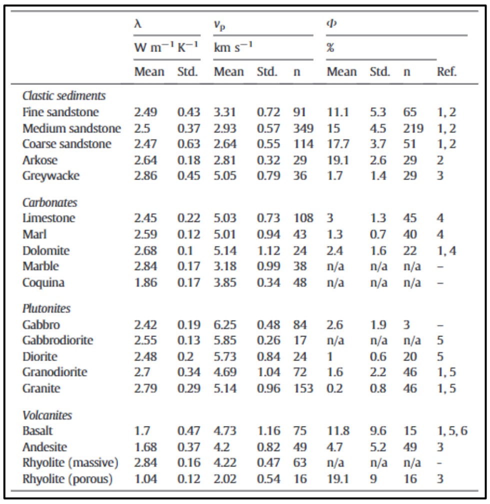

	λ		v_p			Φ			
	$W\ m^{-1}K^{-1}$		$km\ s^{-1}$			%			
	Mean	Std.	Mean	Std.	n	Mean	Std.	n	Ref.
Clastic sediments									
Fine sandstone	2.49	0.43	3.31	0.72	91	11.1	5.3	65	1, 2
Medium sandstone	2.5	0.37	2.93	0.57	349	15	4.5	219	1, 2
Coarse sandstone	2.47	0.63	2.64	0.55	114	17.7	3.7	51	1, 2
Arkose	2.64	0.18	2.81	0.32	29	19.1	2.6	29	2
Greywacke	2.86	0.45	5.05	0.79	36	1.7	1.4	29	3
Carbonates									
Limestone	2.45	0.22	5.03	0.73	108	3	1.3	45	4
Marl	2.59	0.12	5.01	0.94	43	1.3	0.7	40	4
Dolomite	2.68	0.1	5.14	1.12	24	2.4	1.6	22	1, 4
Marble	2.84	0.17	3.18	0.99	38	n/a	n/a	n/a	–
Coquina	1.86	0.17	3.85	0.34	48	n/a	n/a	n/a	–
Plutonites									
Gabbro	2.42	0.19	6.25	0.48	84	2.6	1.9	3	–
Gabbrodiorite	2.55	0.13	5.85	0.26	17	n/a	n/a	n/a	5
Diorite	2.48	0.2	5.73	0.84	24	1	0.6	20	5
Granodiorite	2.7	0.34	4.69	1.04	72	1.6	2.2	46	1, 5
Granite	2.79	0.29	5.14	0.96	153	0.2	0.8	46	1, 5
Volcanites									
Basalt	1.7	0.47	4.73	1.16	75	11.8	9.6	15	1, 5, 6
Andesite	1.68	0.37	4.2	0.82	49	4.7	5.2	49	3
Rhyolite (massive)	2.84	0.16	4.22	0.47	63	n/a	n/a	n/a	-
Rhyolite (porous)	1.04	0.12	2.02	0.54	16	19.1	9	16	3

In this study, the heat flow was calculated using the thermal conductivity from both references (Cermak & Rybach, 1982; Mielke et al., 2017). According to Braun, (2009), the conductivity of the rock decreases as temperature increases, this means that the thermal conductivity in the lower crust is much lower than in the surface. The relationship between the thermal conductivity and the temperature changes was studied by Robertson, (1988) (see appendix 3). For this reason, the thermal conductivity used in this study was the minimum values from each reference (table 3).

Table 3 Thermal conductivity assigned to each tectonic province based on the dominant rocks to estimate the heat flow in the study area.

Tectonic Province	Rockt type	Thermal conductivity (Mielke)	Thermal conductivity (Cermak & Rybach)
Neopterozoic	Clastic carbonate	2.29	0.8
Damara Belt	Granite-gneiss	3.03	1.3
Ghanzi-Chobe Belt	Gneiss	2.44	1.3
Passarge Basin	Sedimentary rock	2.47	0.8
Nosop Basin	Sedimentary rock	2.47	0.8
Kheis Belt	Granite	2.79	1.3
Xade Complex	Gabro	2.42	1.6
Kaapvaal Craton	Granite-gneiss	3.03	1.3
Magondi Belt	Gneiss	2.44	1.3
Limpopo Belt	Metasediment	2.91	1.3
Zimbabwe Craton	Granite-gneiss	3.03	1.3

The result was compared to the mean of continental heat flow value based on the age by Stein, (1995) to determine the heat flow anomaly in the study area (table 4). The value that bigger than average continental heat flow value was considered as the zone that has heat flow anomaly and indicated as the area with the geothermal prospect.

Table 4 Average continental heat flow. (Stein, 1995)

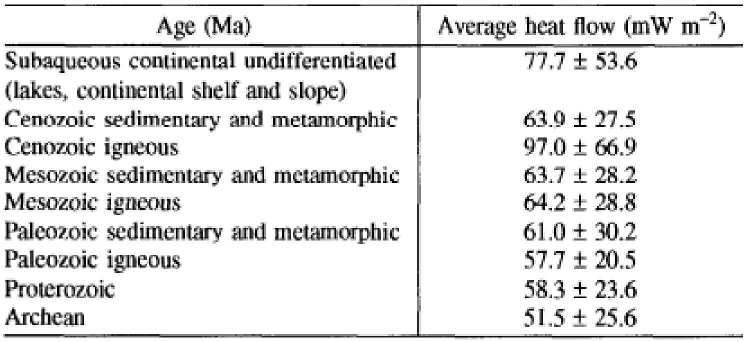

Age (Ma)	Average heat flow (mW m^{-2})
Subaqueous continental undifferentiated (lakes, continental shelf and slope)	77.7 ± 53.6
Cenozoic sedimentary and metamorphic	63.9 ± 27.5
Cenozoic igneous	97.0 ± 66.9
Mesozoic sedimentary and metamorphic	63.7 ± 28.2
Mesozoic igneous	64.2 ± 28.8
Paleozoic sedimentary and metamorphic	61.0 ± 30.2
Paleozoic igneous	57.7 ± 20.5
Proterozoic	58.3 ± 23.6
Archean	51.5 ± 25.6

5. RESULT AND DISCUSSION

5.1. Parameter selection

The method selected in the Curie point depth estimation has very much dependency on the parameter selection. Not only the parameters used in the 1DPSD equation but also in the aeromagnetic input data such as the discrete wavenumber and window size selection.

The method used also required a prior constraint that controls the final result of the CPD selection. In this study, the crustal thickness from (Fadel, 2018) was used as the depth constraint. However, the result produced by each dataset were not able to get a similar value. The most comparable result was the map from 400m and 800m pixel dataset which has an average value difference around 10-15km.

The subsections below are the explanation regarding the parameter selection in this study.

5.1.1. Discrete wavenumber selection

The wavenumber range for each dataset is different; the 200m pixel size is covering wavenumber up to 16 rad/km, for the 400m pixel the highest wavenumber is 8 rad/km and the highest wavenumber for 800m pixel size is 4 rad/km (Figure 14). The CPD maps created by the *pycurious* algorithm from each dataset were calculated using this wavenumber range.

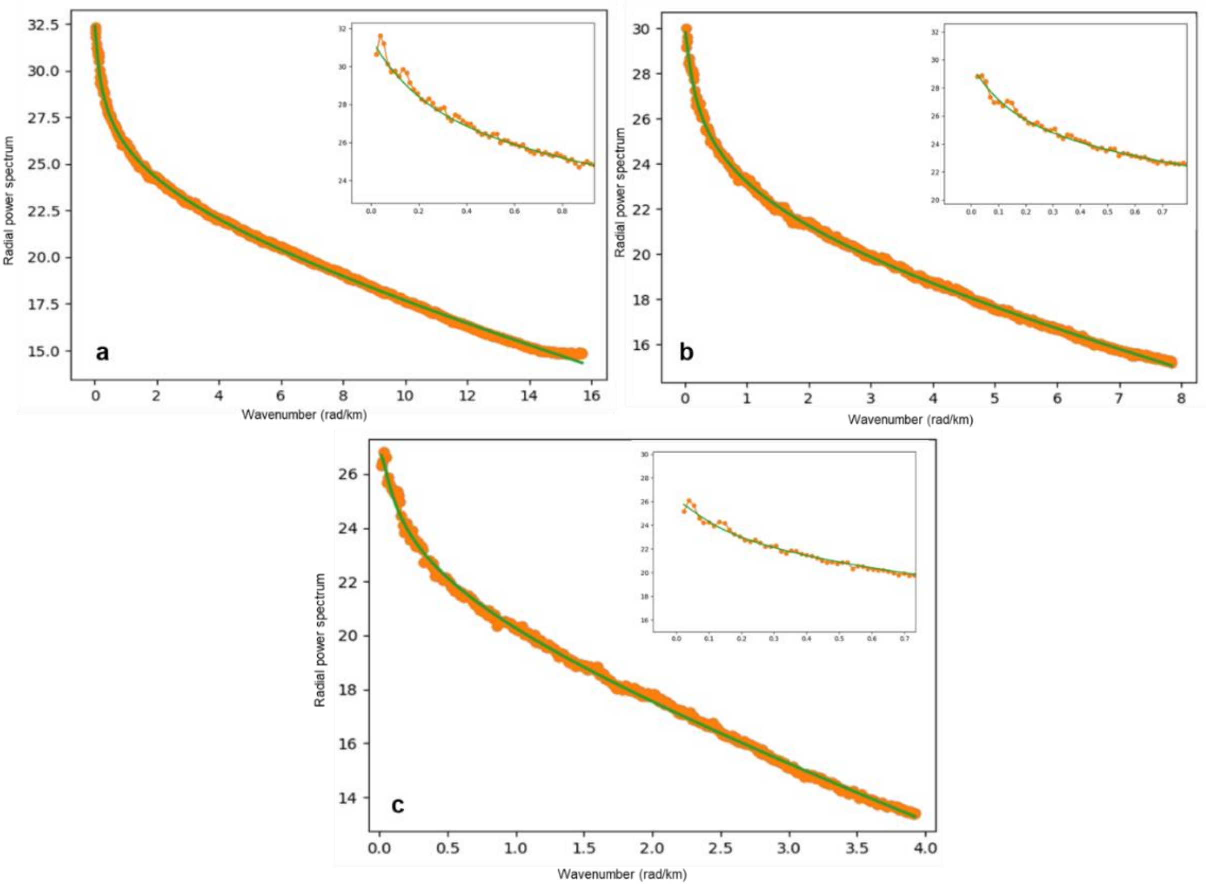

Figure 14 Wavenumber range from each dataset; a) 200m, b) 400m, c) 800m. Small pictures at the top corner of each image are showing the different slopes created at the small wavenumber range of each dataset.

Wavenumber selection using the resampling method influences the result of power spectrum calculation. Not only reducing the wavenumber range, but the slopes generated on the power spectrum of each dataset are also different. According to Bouligand et al., (2009) the slopes that generated by the low wavenumber will lead to different depth values of the bottom of the magnetic source from each dataset. For this reason, the CPD maps were created using the three different datasets to collect all possible CPD estimation from different wavenumber range.

5.1.2. Window size selection

The result shows that different CPD were estimated by different window size used in the same dataset. The influence of the window size variation was assessed by comparing each of the results and examines the power spectrum of each window size. Figure 15 shows that the CPD calculation from three datasets is consistent with the theory for the calculation using a window size of 400km or greater (coherent with the theory from Bouligand et al., (2009)).

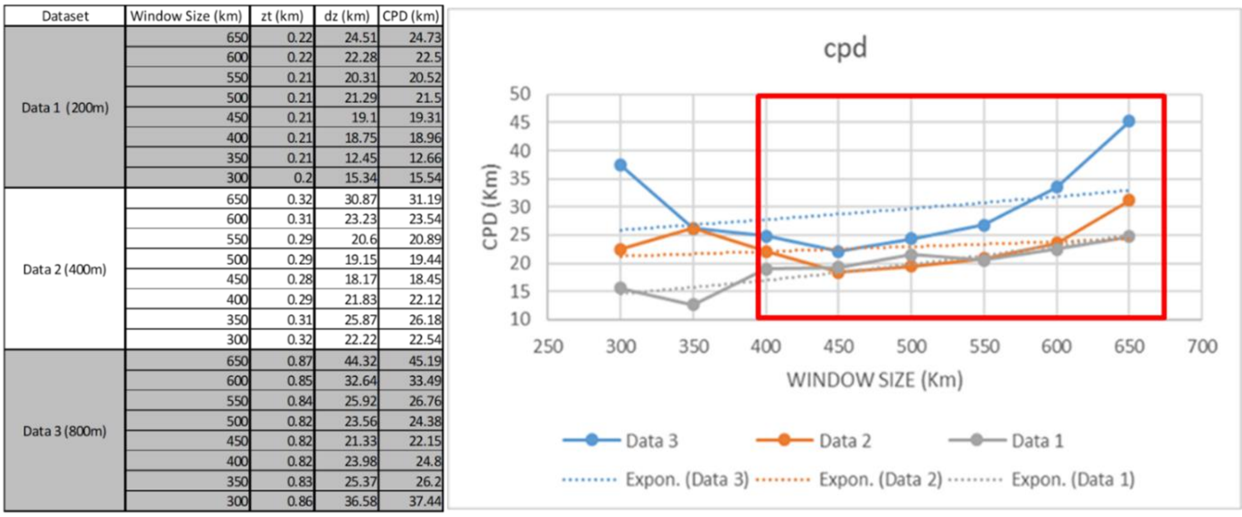

Dataset	Window Size (km)	zt (km)	dz (km)	CPD (km)
Data 1 (200m)	650	0.22	24.51	24.73
	600	0.22	22.28	22.5
	550	0.21	20.31	20.52
	500	0.21	21.29	21.5
	450	0.21	19.1	19.31
	400	0.21	18.75	18.96
	350	0.21	12.45	12.66
	300	0.2	15.34	15.54
Data 2 (400m)	650	0.32	30.87	31.19
	600	0.31	23.23	23.54
	550	0.29	20.6	20.89
	500	0.29	19.15	19.44
	450	0.28	18.17	18.45
	400	0.29	21.83	22.12
	350	0.31	25.87	26.18
	300	0.32	22.22	22.54
Data 3 (800m)	650	0.87	44.32	45.19
	600	0.85	32.64	33.49
	550	0.84	25.92	26.76
	500	0.82	23.56	24.38
	450	0.82	21.33	22.15
	400	0.82	23.98	24.8
	350	0.83	25.37	26.2
	300	0.86	36.58	37.44

Figure 15 CPD calculation from three different datasets using different window size.

Figure 16 shows the lowest wavenumber covered by the different window size applied in the aeromagnetic dataset: the bigger window size, the lower wavenumber covered in the power spectrum calculation. The lowest wavenumber covered is approximately 0.014 rad/km by 650km window size, and the highest wavenumber is around 0.031 by the 300km window size.

The window size of 400km or greater were considered as the suitable size in order to reach the depth of CPD at the very least 40 km (CPD expected based on the value of crustal thickness and the Moho depth model). However, the size of the window needs to be limited. The bigger window size used requires a bigger taper in applying the *pycurious* algorithm to the aeromagnetic data (covering the no data value in a calculation window, see figure 13). To reduce the effect of the taper applied, the window size of 400km was selected as the window size used in this study.

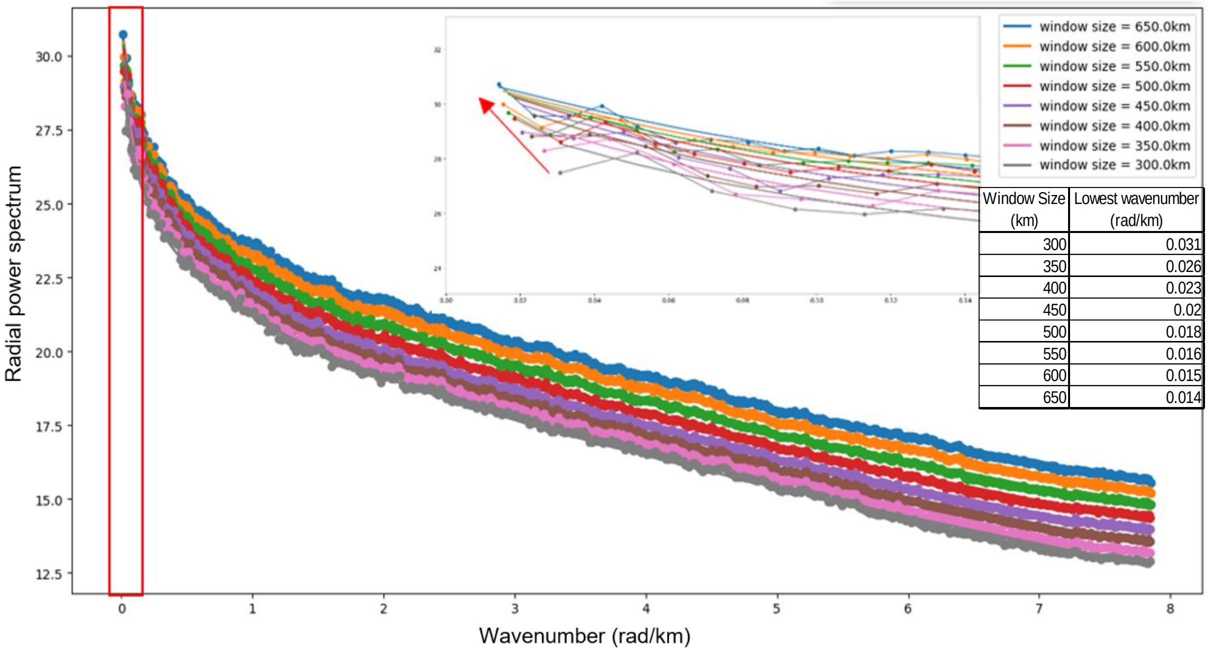

Window Size (km)	Lowest wavenumber (rad/km)
300	0.031
350	0.026
400	0.023
450	0.02
500	0.018
550	0.016
600	0.015
650	0.014

Figure 16 The wavenumber range covered by each window size. The smaller plot is the zoom on the wavenumber range indicated by the red box; the bigger window size recovers the lower wavenumber (the trend is indicated by the red arrow). The table below the plot legends shows the actual value of the lowest wavenumber from each window size.

5.2. Curie point depth estimation

The parameters retrieved from the previous section were implemented to the *pycurious* algorithm for the CPD estimation using the 1DPSD method. Three maps were produced from three resampled images using 400km window size with increments of 50km. The results were compared to the geophysical information to select one of the most realistic result. The result from 400m pixel size dataset was selected as the final map that was used in the remaining analysis of this study.

The more detailed explanation regarding the CPD estimation and the comparison with the previous geology and geophysical information are summarized in the following subsections.

5.2.1. CPD maps

Figure 17 shows the results of CPD and uncertainty map from three datasets produced from the resampled aeromagnetic data.

Table 5 CPD and the uncertainty from each dataset

Dataset	CPD min (km)	CPD max (km)	Uncertainty min (km)	Uncertainty max (km)
200m	0.75	40.46	4.29	11.45
400m	1.15	38.2	4.99	11.22
800m	2.31	40.03	5.63	11.54

The 200 m pixel size dataset results a CPD map that is ranging from 0.75 km to 40.46 km with maximum uncertainty up to 11.45km averaged in 7 km. From the 400m dataset, the value range of the CPD is 1.15km to 38.2km with average uncertainty 7.14 km with a maximum of 11.2 km. The CPD range from 800m dataset is 2.31 to 40.03km (table 5).

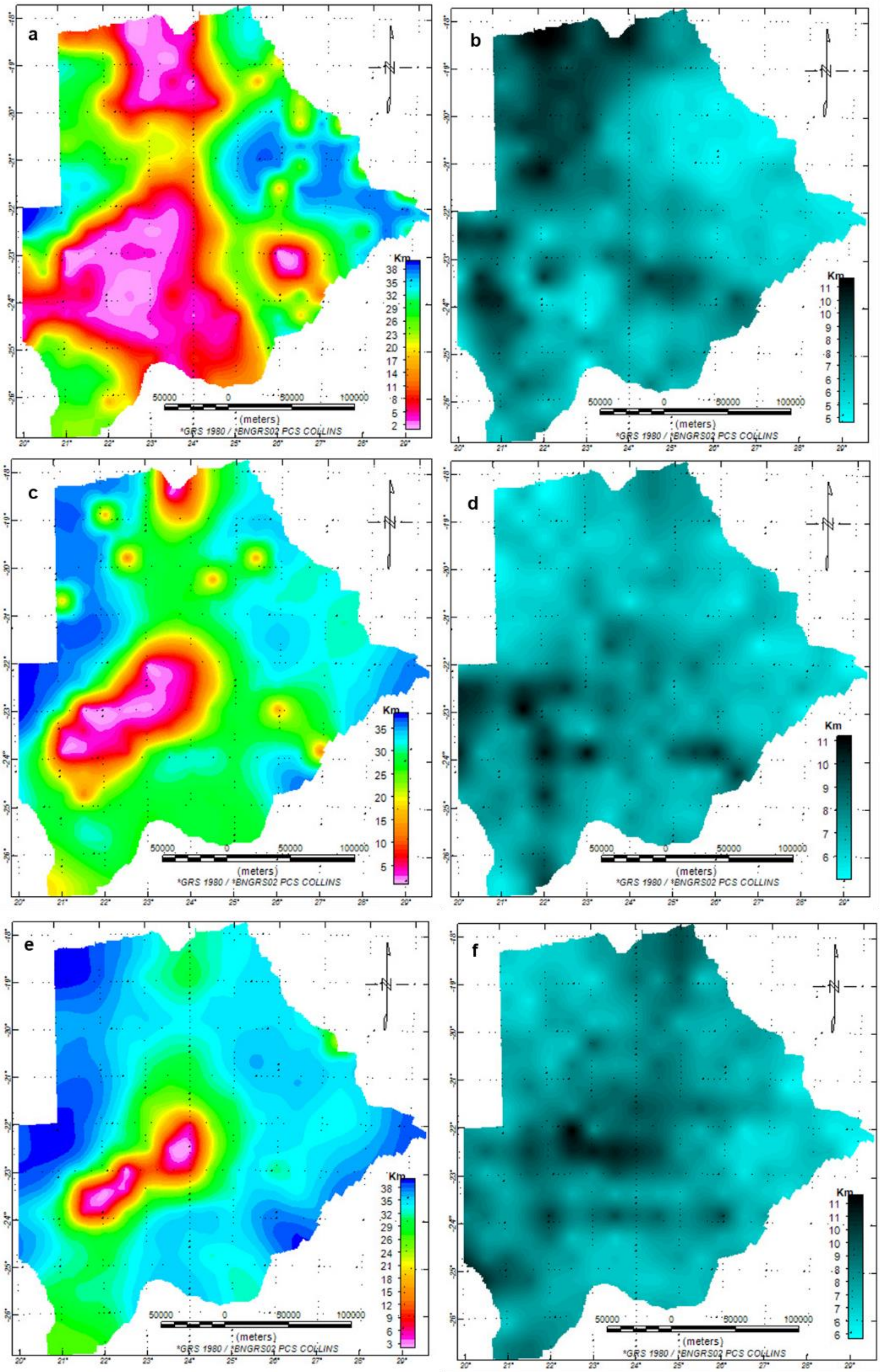

Figure 17 a & b). CPD and uncertainty of 200m pixel size. c & d). CPD and uncertainty of 400m pixel size. e & f). CPD and uncertainty of 800m pixel size.

The results are consistently showing the shallow CPD zone at the central and south-western part of the study area that interestingly shallower than the ORZ which the rifting activity in this zone are agreed by several studies. However, the value of the shallowest CPD from each dataset was observed always overestimating the actual CPD. The common value for the shallowest depth in a CPD study is around 5-10km while this study estimates the shallowest CPD below 1km. For this reason, the depth estimated by this study especially in the shallow zone is not considered as the actual depth.

Comparison with independent geological and geophysical data was performed in order to gather more information regarding the actual CPD of the study area.

5.2.2. Assessment of the CPD results

Technically, the CPD value of the area in the same region should be relatively homogenous. The drastic change usually appears in the boundary of the region. However, if the drastic changes appear in the same region, this value is considered as an artefact. In this study, several artefacts were found in the maps created by this study, especially in the result of 400m pixel dataset (Figure 18). Some assessments were performed to the CPD maps from dataset 400m pixel size dataset to identify what causes the occurrence of the artefacts in these areas.

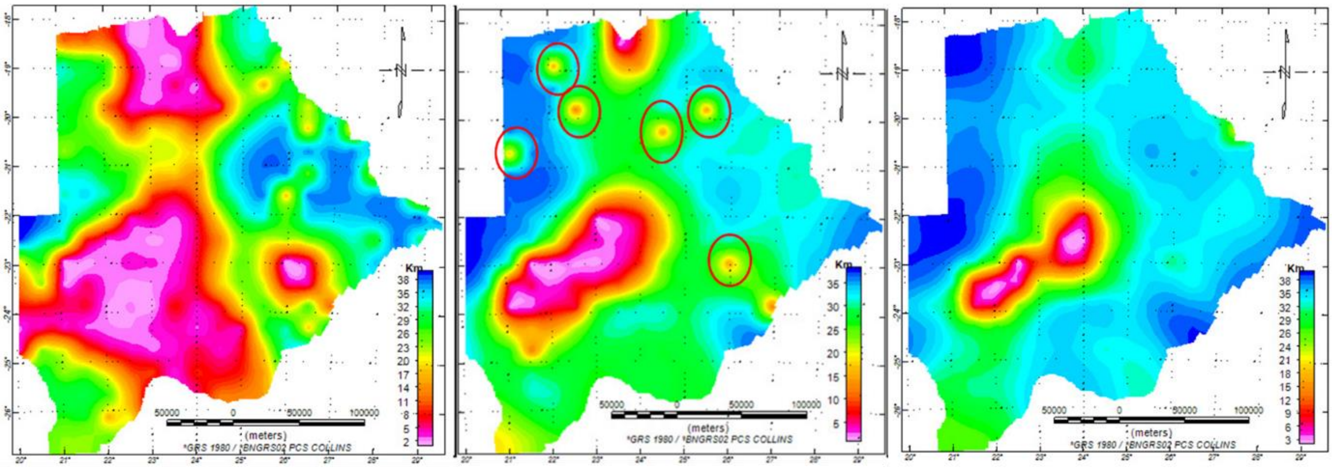

Figure 18 The distribution of artefacts from the 200m, 400m and 800m pixel dataset. The result from 400m has the most artefacts (indicated by red circles).

The first assessment performed was comparing the results of the resampling process from each aeromagnetic dataset. This assessment was executed to compare each other the magnetic data input and observe what cause the appearance of the artefact in a certain area. The magnetic value is taken from a 400km window from each dataset with the location of the artefact being the centroid of the window (Figure 19). Based on this observation, the resampling operation only changes the value of each pixel as the result of the averaging process but keeping the spatial variation of the magnetic anomaly. In another word, the resampling technique did not directly influence the appearance of the artefacts.

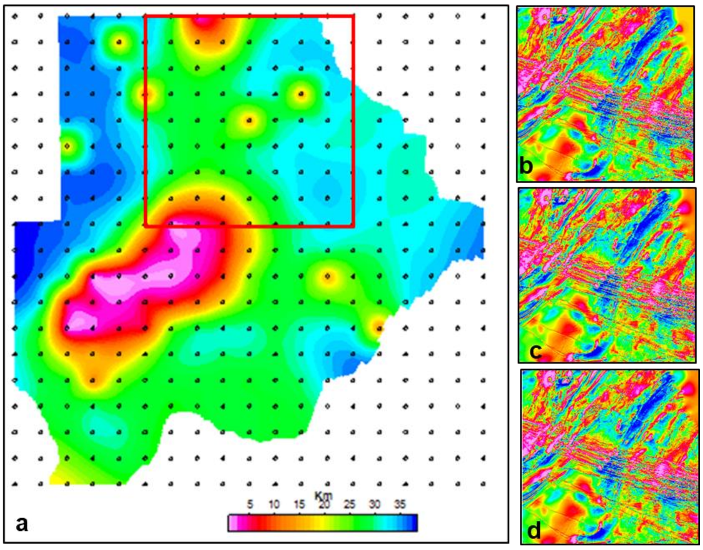

Figure 19 a) CPD map from 400m pixel size dataset, red box indicates the window that used in the CPD calculation with the artefact being the centroid of the window. b) 200m pixel size dataset, c) 400m pixel size dataset, d) 800m pixel size dataset of the red box.

Since there was no clear relation between the resampling effect and the artefacts, further assessments were taken on a single dataset. A window by window comparison from the artefacts with its surrounding was performed. The input data from each window around artefacts were analysed to investigate the possible source of the error in the calculation. According to the observation, there was no significant change between the aeromagnetic data from each window as shown in figure 20. The mean value from each window did not show any variation that might cause the anomaly on the artefact from each surrounding. The mean value from the shallowest CPD at window number 3 does not have the highest and not the lowest magnetic value either (see appendix 5). The CPD vs aeromagnetic plot from the entire study area (Figure 21) also explains that there is no direct relationship between the magnetic value and the estimated CPD of an area.

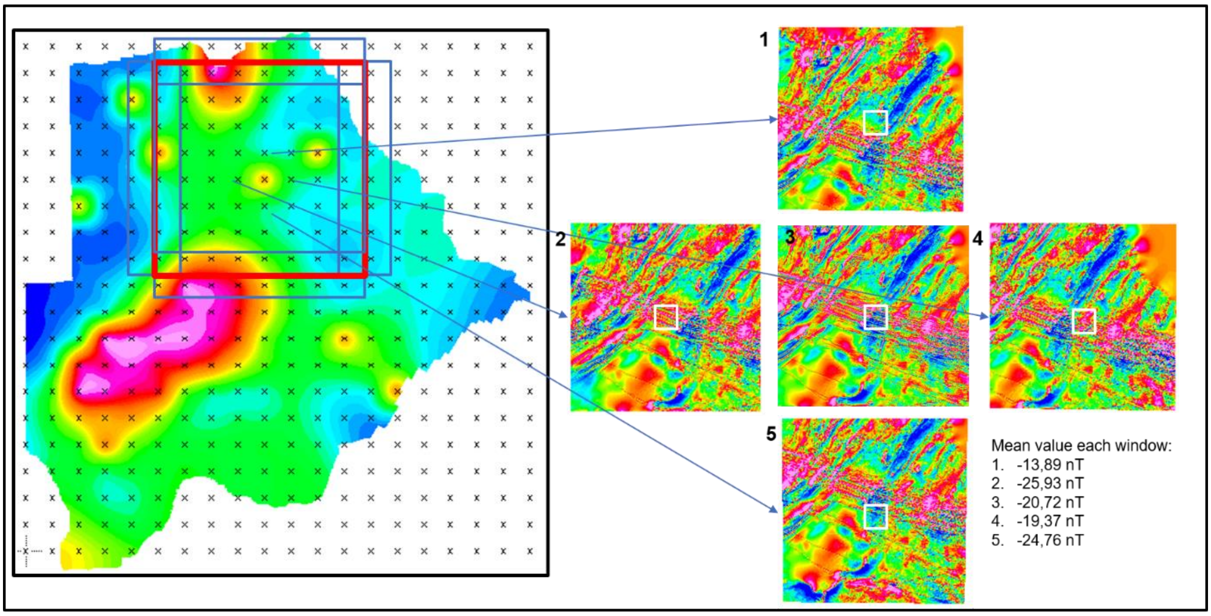

Figure 20 Comparison of the aeromagnetic data input from the artefact and it's surrounding and the mean value of each window. The mean value indicates that there is no direct relationship between the input data and the CPD estimated.

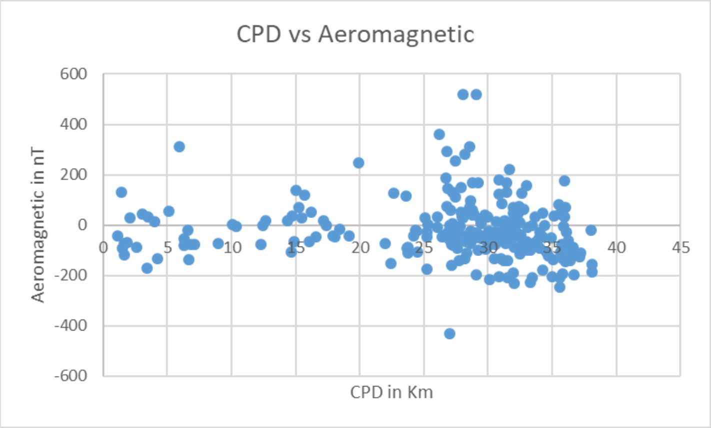

Figure 21 CPD vs Aeromagnetic plot from the entire study area.

Another comparison performed was an assessment of the spectrum created by the 1DPSD calculation. The investigation is taken to understand if there was a mistake during the processing of the dataset. Figure 22 shows the result of the spectrum comparison of the artefact and its surrounding. The slope of the spectrum from the artefact relatively gentle compared to its surrounding. The spectrums indicate that the artefact has shallower CPD compared to its surrounding, referring to the theory by Bouligand et al., (2009).

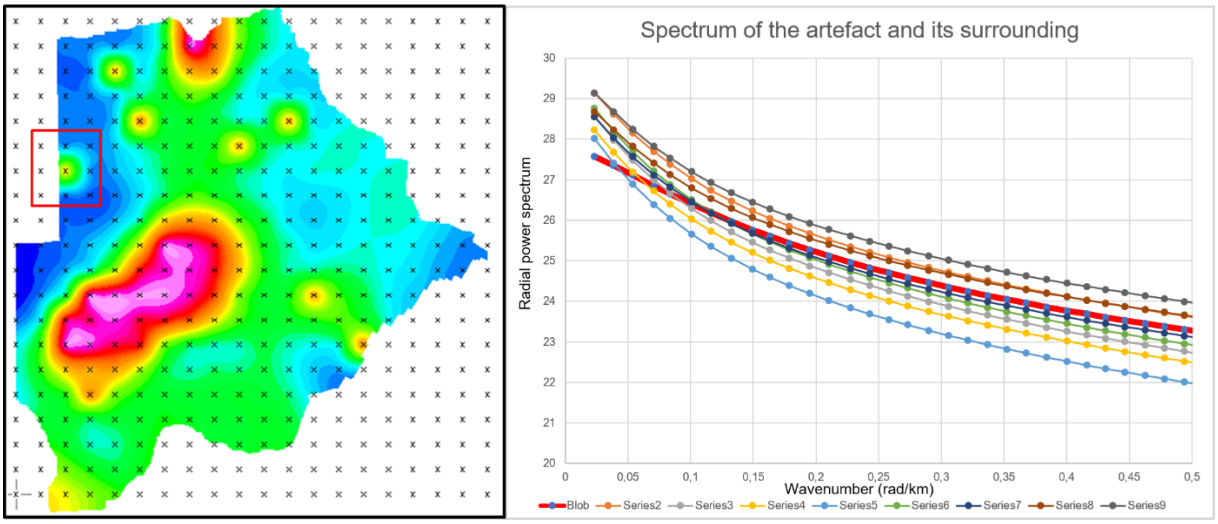

Figure 22 Left) red box shows the location of the spectrum assessed, right) The slope of the artefact (indicated by the red line) has the more gently slope compared to the surrounding.

Another approach performed was shifting the centroid of the 1DPSD calculation horizontally and vertically (see appendix 6 for the results) to investigate the CPD value around the artefacts. The results show that the artifacts still appeared in these versions, this means that these features were not because of a miscalculation but there is some CPD anomaly instead. This was also explained by the artefacts that are shown in the south-eastern part of the 400m pixel dataset were clearly indicated as an anomaly in the 200m pixel dataset. This anomaly might also be related to the 2017 earthquake, the event that was caused by a normal fault oriented NW-SE in this area (Midzi et al., 2018). The epicentre of the earthquake located close to this artefact. Based on this finding, a new CPD map was generated with a smaller increment (25 km) to see the more detailed distribution of shallow CPD around the artefacts (Figure 23a).

The distribution of these artefacts coincidence with the result from the previous study by Leseane et al., (2015). As indicated by the blue polygon on figure 23b, the artefacts appear to be consistent with the map from the previous study. The artefacts that are showing a shallow depth from this study were also found in the previous study. Additionally, there is an artefact from this study that located in the south-western part of the previous study area that consistent with the extent of Ghanzi-Chobe belt in this area.

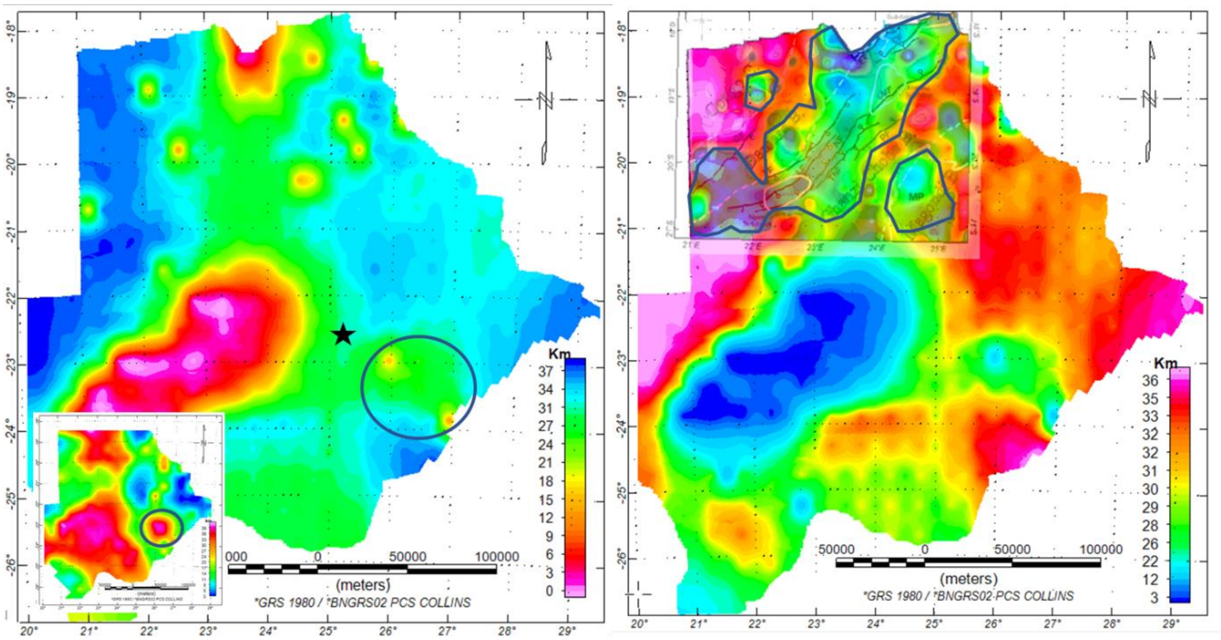

Figure 23 a) CPD map from 400m pixel size using increment 25km. The artefacts in the south-eastern part indicated as an anomaly in the result of 200m pixel size dataset. b) reversed color of CPD map overlaid with the previous model by Leseane et al., (2015), blue polygon indicates the similarity between the artefacts from this study and previous study. The black star indicates the epicentre of the 2017 Botswana earthquake.

5.2.3. Correlation between CPD and near-surface heat flow

Many of the studies on CPD includes the discussions the correlation between the CPD and surface temperature, so did this study. This comparison was performed to validate the result of the CPD estimation. In general, the correlation between high heat flow with shallow CPD is positive (Okubo et al., 1985; Tanaka et al. 1999).

In this study, the CPD models were compared to the near surface heat flow information from 14 wellbores drilled across Botswana. Table 6 displays the CPD value from each dataset at the location the wellbore drilled and compared to the heat flow value.

Table 6 The CPD result from each dataset and the near-surface heat flow from the wellbore

Site	Name	heat flow from wellbore (mW/m2)	CPD from dataset 200m (Km)	CPD from dataset 400m (Km)	CPD from dataset 800m (Km)
1	Lobatse	30	20.46	29.75	34.07
2	Molopo Farms	45	5.19	28.04	34.34
3	Mmamabula	42	14.76	24.25	35.32
4	Maboane	35	5.35	30.72	35.57
5	Moropule	52	31.4	31.01	34.04
6	Gope	49	9.52	12.34	12.13
7	Selebi-Phikwe	53	36.83	32.35	34.38
8	Francistown	37	33.57	30.69	34.35
9	Bushman Mine	65	32.53	31.36	35.33
10	Orapa	60	37.77	32.13	34.24
11	Tshane	76	1.44	5.43	6.64
12	Mabuasehube	25	19.94	28.44	31.52
13	Kachikau	56	19.03	19.66	31.97
14	Ngamiland	60	26.43	31.66	37.32

Figure 24 shows the correlation between the CPD estimation for each dataset and the near-surface heat flow from wellbore dataset. Not any of the result has a good correlation, the R^2 of the results were very low from any dataset. There was no result that has R^2 bigger than 0.2. However, the trend of the linear regression of the dataset 400m and 800m pixel size are relatively coherence with the well-known theory, the shallower CPD the higher heat flow.

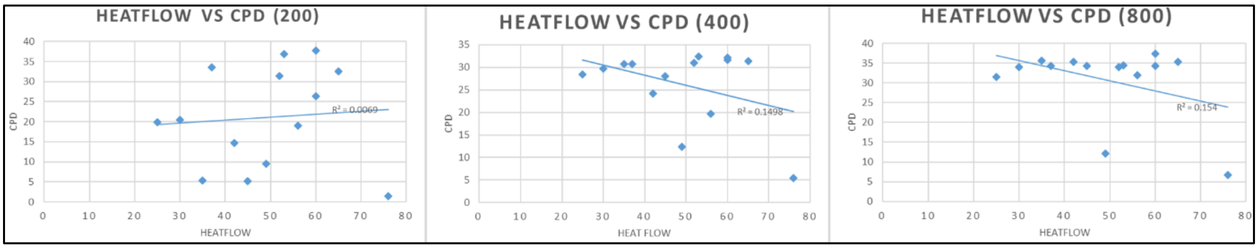

Figure 24 CPD vs heat flow correlation from each dataset, the dataset of 400m and 800m are showing a positive relationship between the shallow CPD and high heat flow. The R^2 values were below 0.2 in any dataset.

The four wells that create the poor correlation are located in a complex geological condition from different tectonic provinces as shown by figure 25 below. This might have an impact on the heat flow measured by the wellbores and caused the poor correlation.

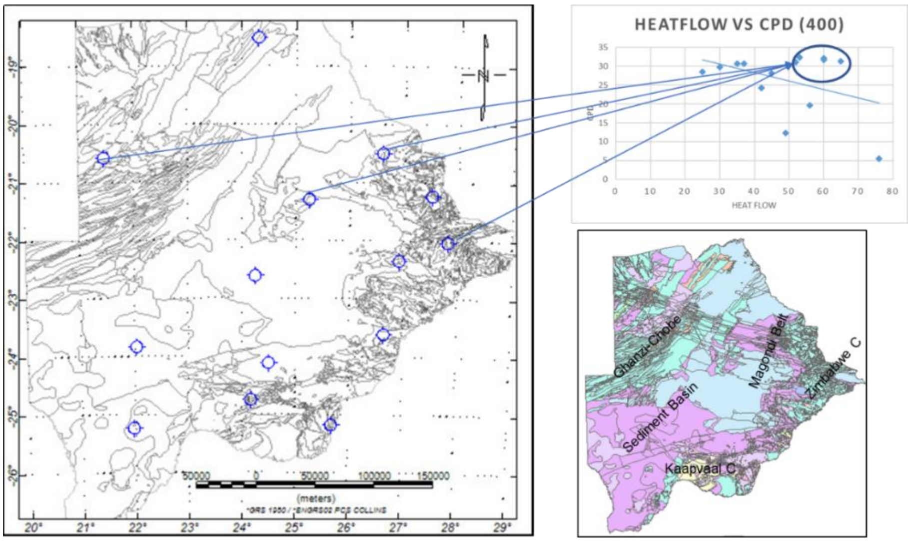

Figure 25 The location and geological condition of four wells that have poor CPD and heat flow correlation.

The correlation between CPD and heat flow were increased significantly after removing the four well that has a poor correlation. The R^2 of the plot from any dataset rises drastically (see figure 26). The trend of the result from 200m dataset has corrected and the R^2 from 400m and 800m dataset increased to 0.5374 0.7699.

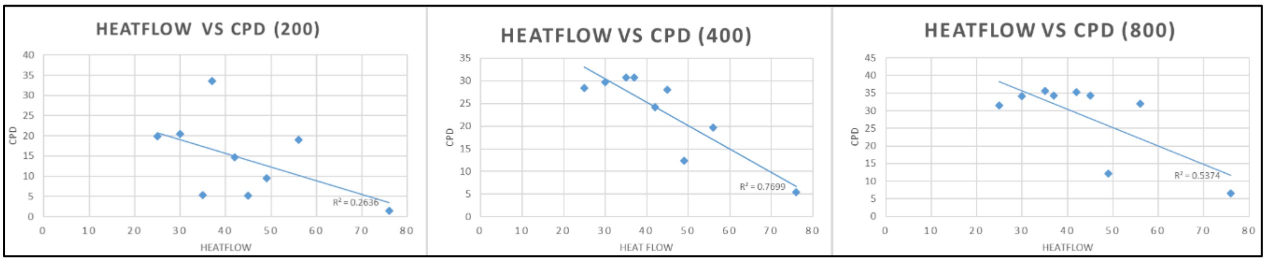

Figure 26 CPD vs heat flow correlation from each dataset after removing several wells with poor correlation. The R^2 values were increased significantly up to 0.7699.

5.2.4. Comparison with the previous studies.

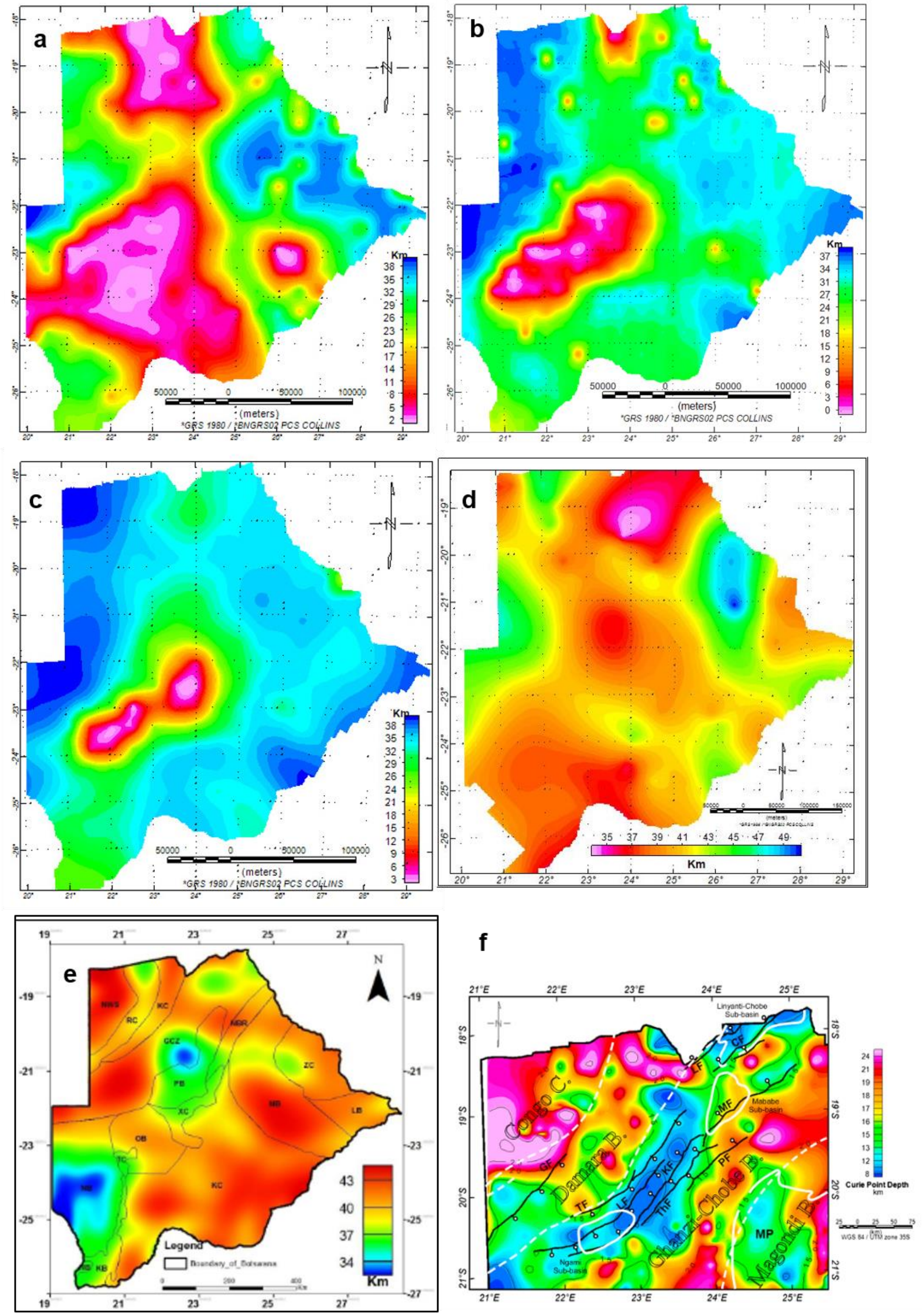

Figure 27 Comparison with previous geophysics studies. a-c) CPD result from 200m, 400m and 800m dataset in this study, d) the crustal thickness model by Fadel (2018). e) Moho depth model by Chisenga (2015). f) CPD at Okavango Rift zone by Leseane et. Al (2015).

There are several geophysical models available in Botswana, such as Moho depth, crustal thickness and CPD model. Figure 27 displays the CPD result and the previous geophysical models available. To select the final CPD model, the results from this study were compared to these models. The shallow CPD zones appeared in the thin crust and shallow Moho areas.

The results of the comparisons show that the CPD map created from 400m pixel dataset is the most realistic result. This conclusion was drawn based on the consideration that the result produced by the 400m pixel dataset has the most correlation with the geophysical models used for comparison. The CPD map from 400m pixel size was used for further analysis in this study. The results of each comparison are explained in the sub-section below.

- **Comparison with crustal thickness model by Fadel, (2018) and Moho depth by Chisenga, (2015)**

Despite the fact that the depth prior constraint of 45km was already applied to the algorithm, the result could not get the same depth of the crustal thickness and Moho depth model. This was due to the size of the window used in calculating the power spectrum of the aeromagnetic data, the deepest feature covered were approximately tenth times smaller of the window size as explained by Bouligand et al., (2009).

Based on the spatial distribution, the model from the 200m dataset are quite similar to the crustal thickness model while the result from 400m and 800m dataset seems to be less similar. Apart from that, all the shallow CPD in these maps regularly appear in the thinner crust. Despite having a bigger difference from the spatial comparison, the 400m and 800m dataset were showing less value difference between the CPD and crustal thickness which are around 10-15km in most of the parts except on the shallow zone.

Figure 28 and 29 shows the statistics and the distribution of the value differences between the CPD and the crustal thickness from each dataset. The biggest difference in any maps always situated in the very shallow CPD zones.

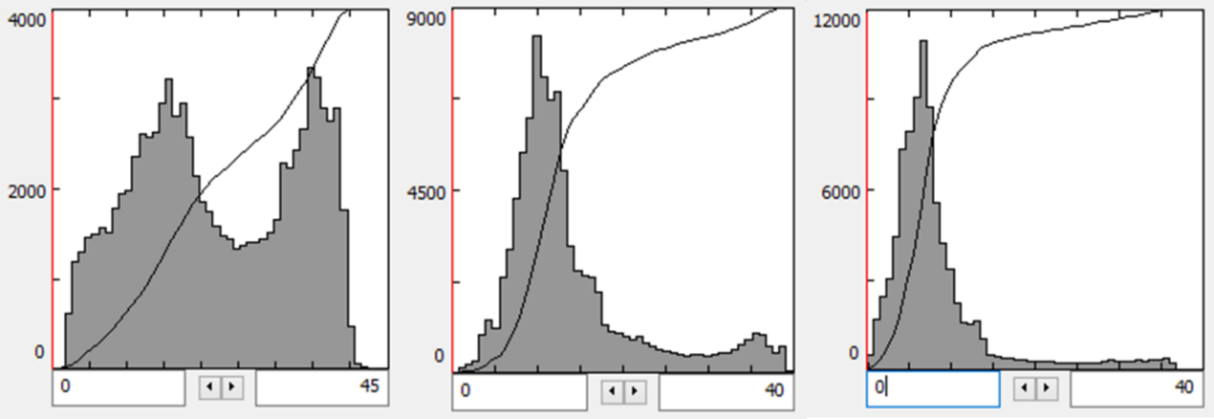

Figure 28 The dataset of 400m and 800m has less value difference as displayed by the statistic of depth differences between the crustal thickness and CPD (x-axis is the value differences in Km; y-axis is the pixel count). Left) CPD from 200m dataset, middle) 400m dataset, right) 800m dataset.

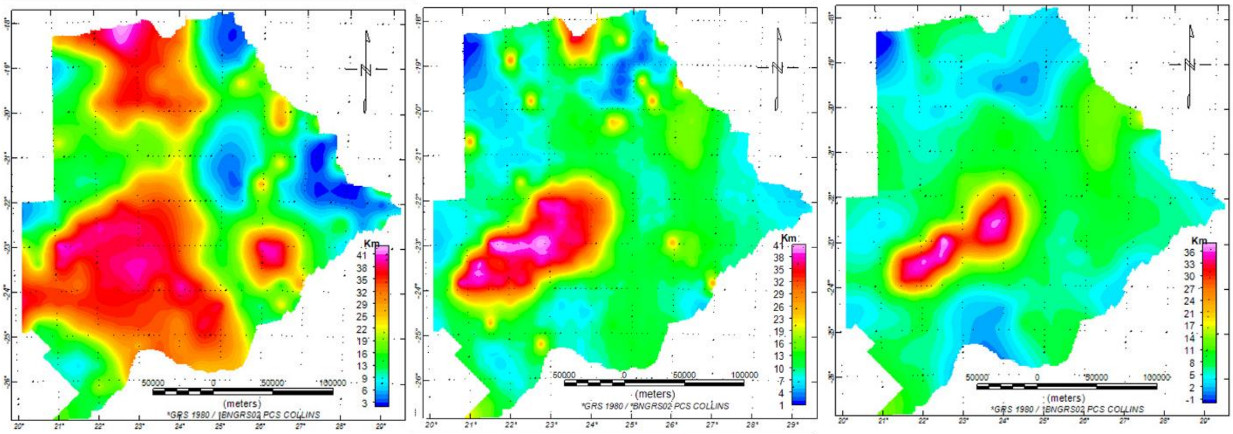

Figure 29 The distribution of value differences between CPD result and crustal thickness model, the higher value difference caused by the shallower CPD. (Left: CPD200, centre: CPD400, right: CPD800)

The CPD result was also compared to the Moho depth model from Chisenga, (2015), in order to get another insight regarding the distribution of the CPD and the thinning crust. Comparing the result with this model also give a comparable spatial distribution between the shallow CPD and thinner crust in the study area, except for the result from 200m pixel dataset. As explained earlier, the window size selection limits the depth of the CPD and could not reach the depth of Moho just like in the previous comparison.

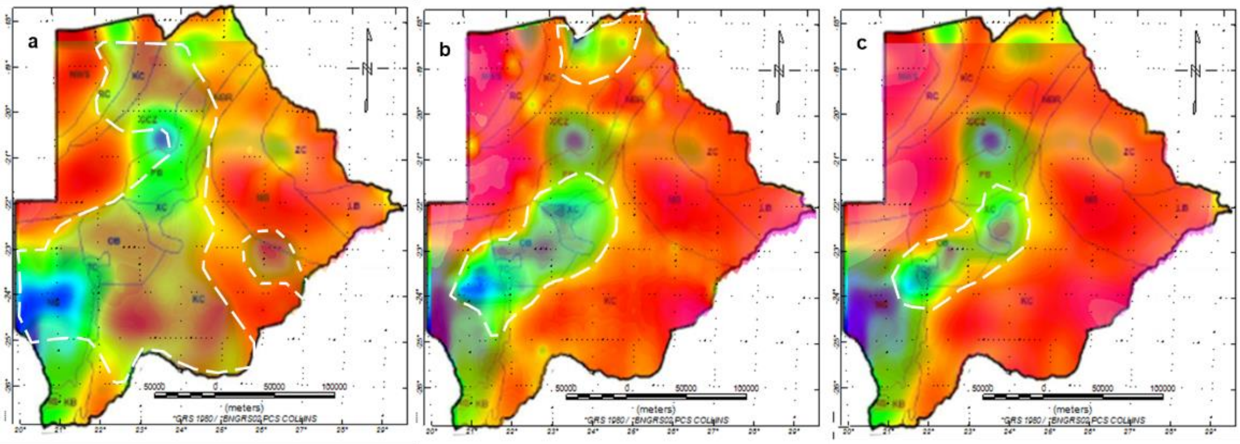

Figure 30 The CPD result overlaid with the Moho depth model from Chisenga, (2015). The white dashed line indicates the spatial distribution of shallow CPD from each dataset. a) CPD200 vs Moho depth. b) CPD400 vs Moho depth. c) CPD800 vs Moho depth.

The result from both comparisons demonstrates that the CPD was always shallower the crustal thickness and Moho depth model. Apart from the very shallow zone, the CPD shallower than the crustal thickness by 10-15km. According to previous CPD studies, this value is within the range of the result they produced. Several examples are; Li et al., (2010) estimated the difference between the Moho depth and CPD in southern China approximately 7km and the Moho of the Arabian shield is estimated deeper by 10-15km from the CPD by Aboud, Alotaibi, & Saud, (2016). Further analysis required to get a better understanding regarding the factor that differentiates the CPD from the crustal thickness and Moho.

- **Comparison with CPD from 3-D inversion method in ORZ by Leseane et al., (2015)**

The more detailed CPD calculation using 3-D inversion method in Okavango Rift Zone (ORZ) by Leseane et al., (2015) was used as the comparison of the result from this study. Figure 27 d, e and f show that the shallow CPD in the ORZ can also be seen in any result of this study. This is consistent with the result from a 3-D inversion that found the dyke swarm which indicates the rifting activity in this zone caused the lifted heat that influences the shallow CPD.

The CPD result from 200m and 400m has relatively close to the result estimated by the previous study, while the depth of shallow CPD in ORZ from 800m was too deep. Between 200m and 400m pixel dataset, the result from 400m pixel size dataset appears to be the closest result with the previous study with the shallow CPD around 4-18km.

This comparison was also performed to get information regarding the actual depth of the CPD in the study area. As previously stated, the limitation of the method used for the CPD estimation in this study is overestimating the shallower CPD. On the other hand, the 3-D inversion method executed by Leseane et al., (2015) recognized as the better method to map the CPD for a small area in detail. They found areas with CPD as shallow 8km which is very close to the previous study about the heat source in EARS by King & Metcalfe, (2013) at approximately 6km. According to this, the shallowest CPD in the Okavango Rift Zone is expected to be around 8-10km and not lower than 5km as shown by the results of this study. However, the study by Leseane et al., (2015) only cover the small part in northern Botswana. The actual depth for the shallow CPD in the central and southern part of the study area (which are estimated shallower than in the ORZ) remain questionable and requires a further detailed study.

5.2.5. The relationship between the CPD and geological setting of the study area

The result was also compared to the basement geological map from Chisenga, (2015) to understand the relationship between the shallow CPD and the tectonic activity of Botswana (Figure 31). According to the author, there is a possibility of the reworking of the extension or rifting activity in the southern part of Botswana that indicated by several mafic intrusion rocks formation. The shallow CPD coincidently appear in these weak zones along the Ghanzi-Chobe Belt to the Nosop Basin in the south-western part of the study area.

In the northern part, the result of this study was also able to distinguish the shallow CPD at this area. As explained by Leseane et al., (2015), the extent of shallow CPD in the northern part of Botswana (ORZ) is related to the Ghanzi-Chobe belt and so did the result of this study.

The result also identifies that the extent of the shallow CPD zones in southern Botswana is coherent with the weak zone distinguished by the basement geology map. The first obvious observation was the very shallow CPD in the middle of Botswana fell into the part of the sedimentary basins (Passarge and Nosop Basin) which intruded by Xade complex and Okwa block.

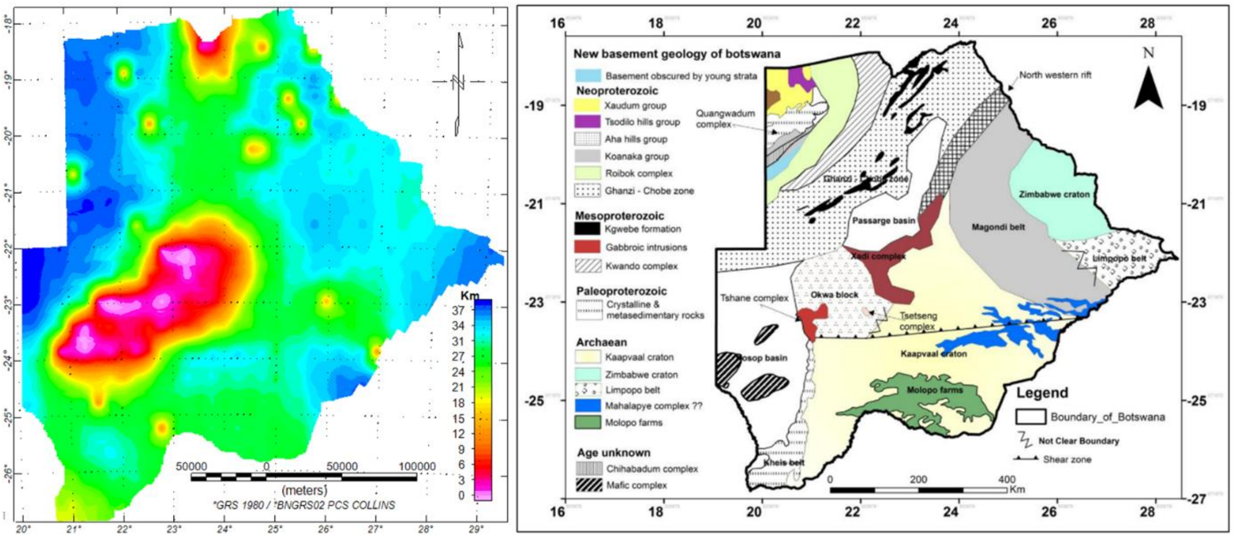

Figure 31 Left) the final CPD map created from the 400m dataset. Right) Basement geology map of Botswana (Chisenga, 2015)

Another shallow CPD zones that might be related to the old intrusive rock were in the south-eastern part of the study area, Mahalapye complex and Molopo farms represented by the shallow CPD around 20-25 km. The shallow CPD zones have also appeared along the extent of Palala fault that broke the northern part of Kaapvaal Craton. Figure 32 highlights the correlation between shallow CPD zones with the geology features that indicate the weak zones in Botswana.

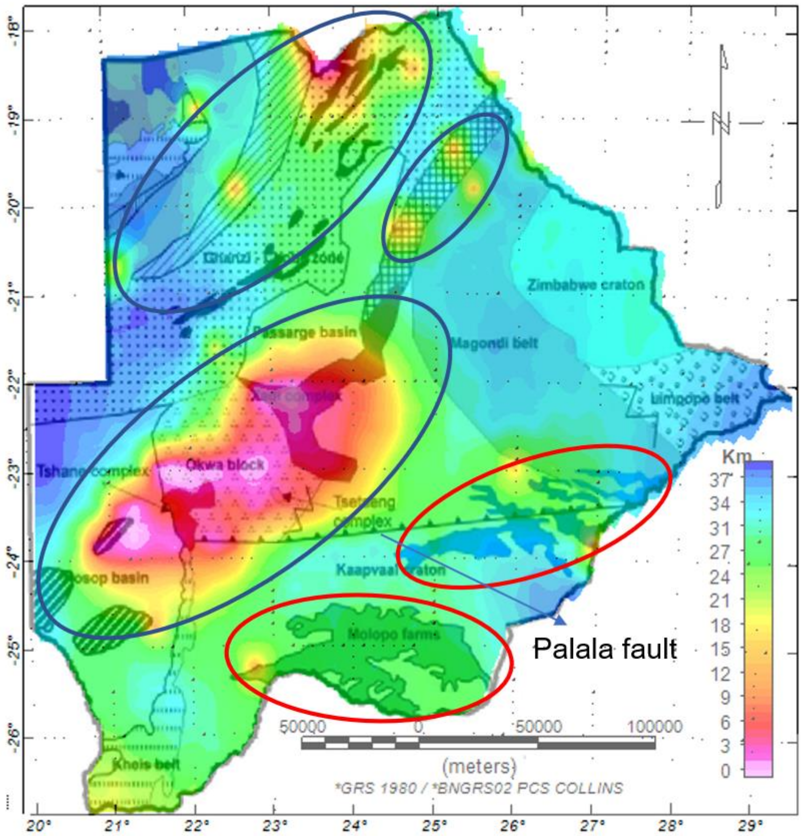

Figure 32 Correlation between shallow CPD zones with geological features in the basement. Red circle indicated that shallow depth related to the old intrusive rock and the blue circle indicates the shallow depth related to the younger intrusive rock.

The deeper CPD were found in the cratonic areas. In the eastern part, the deep CPD situated in the Zimbabwe Craton and the old belts in this area. Meanwhile, in the southern part, the deep CPD located the Kaapvaal Craton that was stable and not intruded by a younger rock or affected by the Palala Fault. An interesting result was found in the north-western and western part of the study area, the very deep CPD found in the area that suggested as the Ghanzi-Chobe Belt and the younger products from Damara Belt by the geology maps. This deep CPD zone is also supported by the appearance of the thicker in this area. There was a study by Singletary et al., (2003) that explain that the north-western part of the study area is the part of Congo Craton, this could be the alternative explanation of the deeper CPD in this area. Further study to review the boundary of the Congo Craton in this area might be necessary.

Comparison with the basement geology of Botswana explains that the occurrence of the shallow CPD from this study is very much related to the geological setting of the area. The weak zones that indicated by a fault and the lithology were represented by the shallow CPD. Furthermore, the CPD in the older intrusive formations (Molopo farm and Mahalapye complex) are relatively deeper than the CPD in the younger intruded rock, this might also be an indication that the continuation of the recent rift (EARS) caused the shallower CPD estimated in Ghanzi-Chobe and the sedimentary basins.

5.3. Heat flow calculation

In this study, the heat flow was calculated using the thermal conductivity value from two different references. The first was from Mielke et al., (2017) and the other was Cermak & Rybach, (1982).

The first heat flow map was produced using the thermal conductivity value from Mielke et al., (2017). The result shows the lowest heat flow 34 mW/m² and the highest is beyond 400 mW/m². The second heat flow map was created using the thermal conductivity from Cermak & Rybach. The lowest heat flow calculated is approximately 18 mW/m² and the highest is beyond 300 mW/m². Both of the results show the very high heat flow in the very shallow CPD zones.

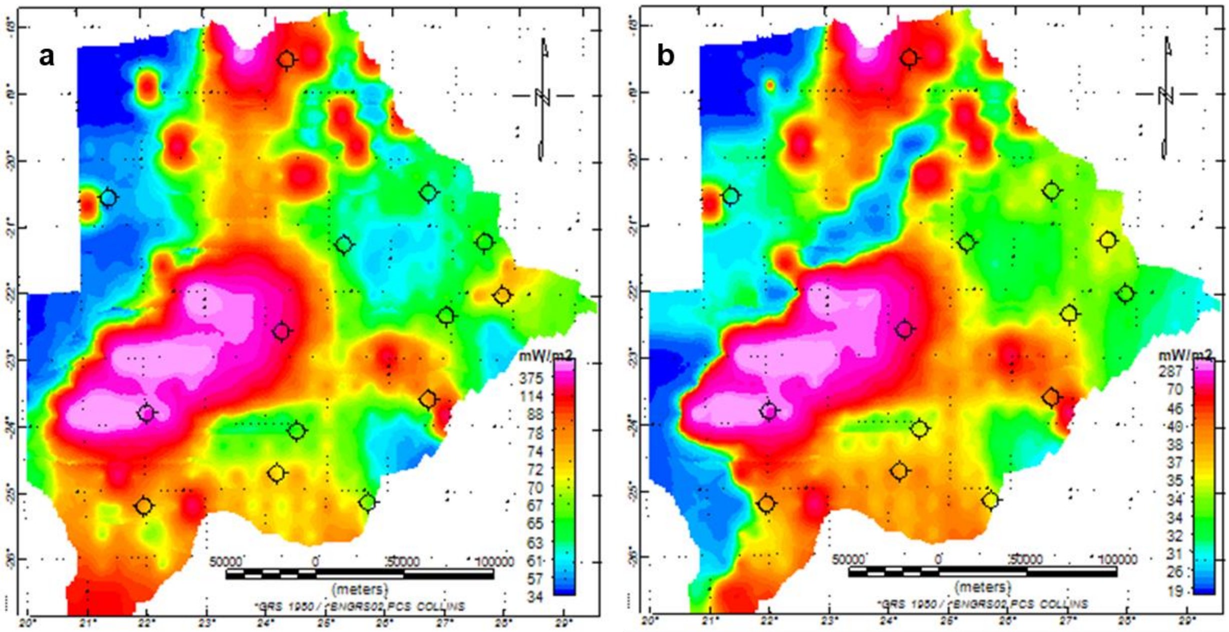

Figure 33 Heat flow map using thermal conductivity from; a) Mielke et al., (2017) and b) Cermak & Rybach, (1982). The circles indicate the wellbore location.

The heat flow from wellbore was used as the validation of the calculation. Figure 34 shows the comparison between the estimated heat flow from this study and the heat flow from the wellbores.

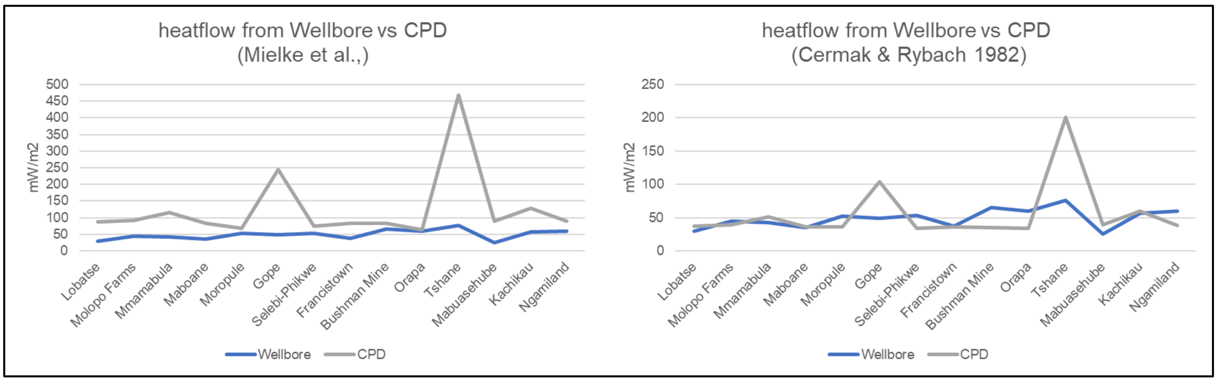

Figure 34 Comparison between the heat flow from wellbores and CPD using two different thermal conductivity references. The result of the second calculation using thermal conductivity from Cermak & Rybach (1982) relatively comparable with the heat flow from wellbore information.

The result of the first calculation was overestimating the heat flow from the wellbore, this might be caused by thermal conductivity gathered from Mielke et al., (2017) was the thermal conductivity in the surface measurement at ambient conditions (0.1Mpa and 25^{0}C). However, the result of the heat flow estimation using thermal conductivity value from Cermak & Rybach, (1982) was nicely comparable with the wellbore information compared to the first calculation. The heat flow values estimated matched the values from the wellbore in several locations such as Maboane and Kachikau.

Based on the comparison with the heat flow from the wellbore, the heat flow map that used for the geothermal prospect identification was the map that produced using thermal conductivity value from Cermak & Rybach, (1982).

5.4. The relationship between CPD, heat flow and crustal thinning theory

The relationship between the shallow CPD and high heat flow with the crustal thinning theory explained in this subsection. The result shows that the occurrence of the shallow CPD and high heat flow has a strong relationship to the crustal thinning theory. The depth variation of the CPD commonly appears in the thin crust area based on the crustal thickness model by Fadel, (2018).

Figure 35 shows the variation from two sections that display the relationship between the CPD, heat flow and the crustal thickness. The sections were taken in the direction of NW-SE perpendicular with the trend of the belts that produces shallow CPD to get the better illustration regarding the variation of the crustal thickness in the subsurface.

The first section was taken in the Okavango Rift Zone to investigate the structure of Ghanzi-Chobe belts and its implication to the CPD and the heat flow. The variation of the CPD and heat flow relatively similar to the thinning crust area. The shallowing CPD in the south-eastern part of the section was not indicated by the crust model, this is due to the lack of data was used that caused the variation by the CPD was not represented in the crustal thickness model.

The relationship between the CPD and crustal thickness in the middle part of Botswana is represented by line 2. This shallow CPD and thin crust in this zone are related to the geologically weak zone in the sedimentary basins that interpreted as the continuation of EARS in the center to the south-western part of the study area.

Overall, the two sections taken give a better interpretation regarding the relationship between the CPD and heat flow variation with the crustal thickness model. This was also supported by the fact that these zones were located in the geologically weak area in the study area as the result of rifting or extension activity at the Ghanzi-Chobe belt and the sedimentary basins.

To conclude, the crustal thinning activity is one of the major factors that lifts the Curie point depth of the study area.

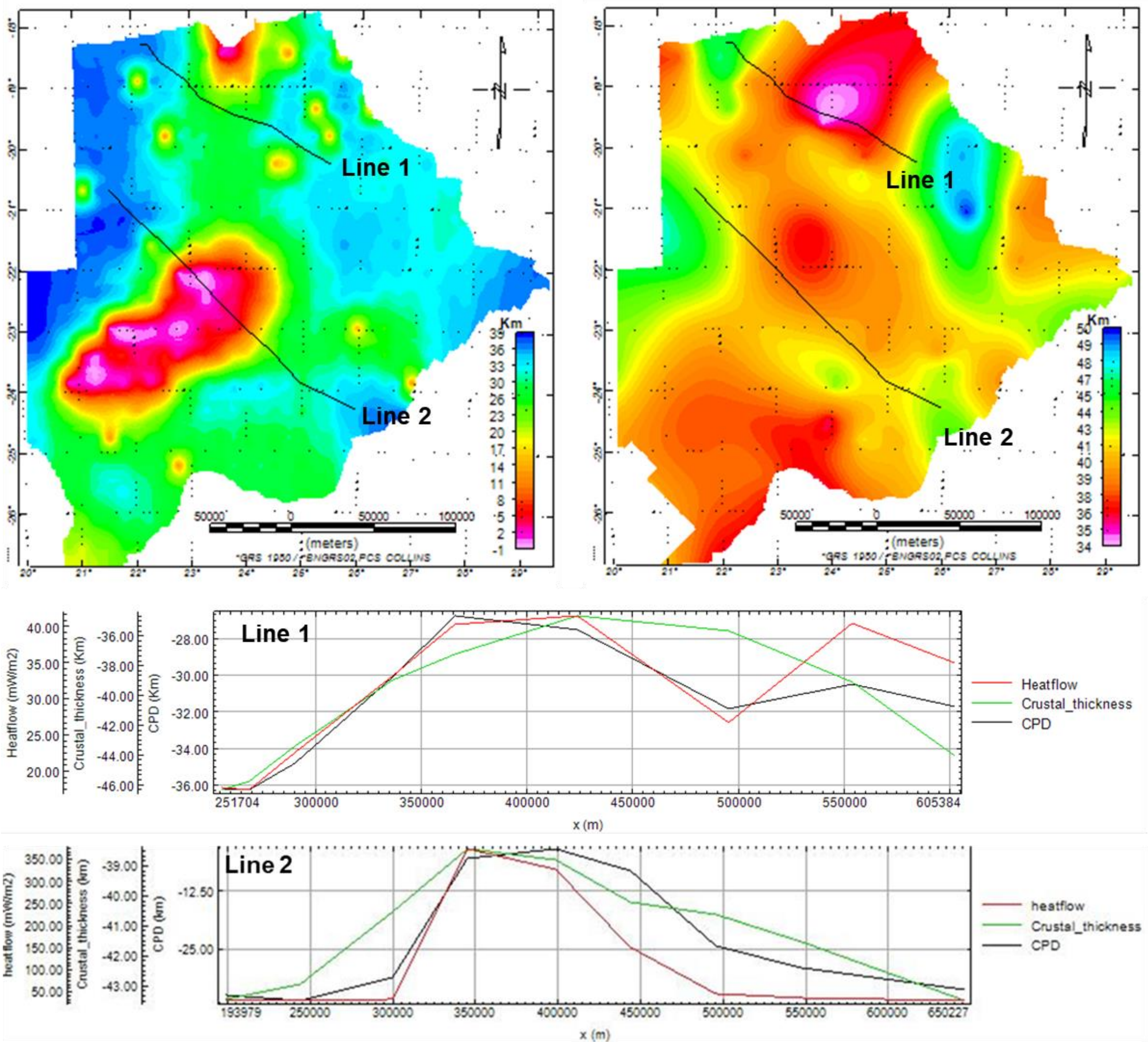

Figure 35 Top images are the sections overlaid to the CPD and crustal thickness map. Bottom images are the cross-section that contains information of CPD, crustal thickness and the heat flow. The sections were drawn perpendicular with the trend of the belts that caused the shallow CPD in the study area. The sections display that the variation of shallow CPD and high heat flow are coherent with the thinner crust.

Referring to the strong relationship between the CPD and the crustal thickness model, the CPD from this study could be supporting evidence of the crustal thinning theory to explain that suggest the continuation of the EARS system in the study area is extended to the center and southern part of Botswana.

5.5. Geothermal prospect identification

The geothermal prospect in the study area identified by the looking to the anomalous heat flow value that higher from the global average continental heat flow. According to the regional tectonic information, the study area consists of the continental province with age Archean-Neoproterozoic. This means that the global average continental heat flow in the study area is ranging from 51.5 - 61.0 mW/m^2. The zones with heat flow value above this range were considered as the area that has a geothermal prospect.

Based on the anomalous heat flow, several areas were delineated as the geothermal prospect area as shown in figure 36. These areas were divided into 2 different zones based on the geological setting. The first zone is the high heat flow area that located along the Ghanzi-Chobe Belt and the sedimentary basins and the other is in the south-eastern part of the study area that related to the Early Proterozoic shear zone, represented by Palala fault.

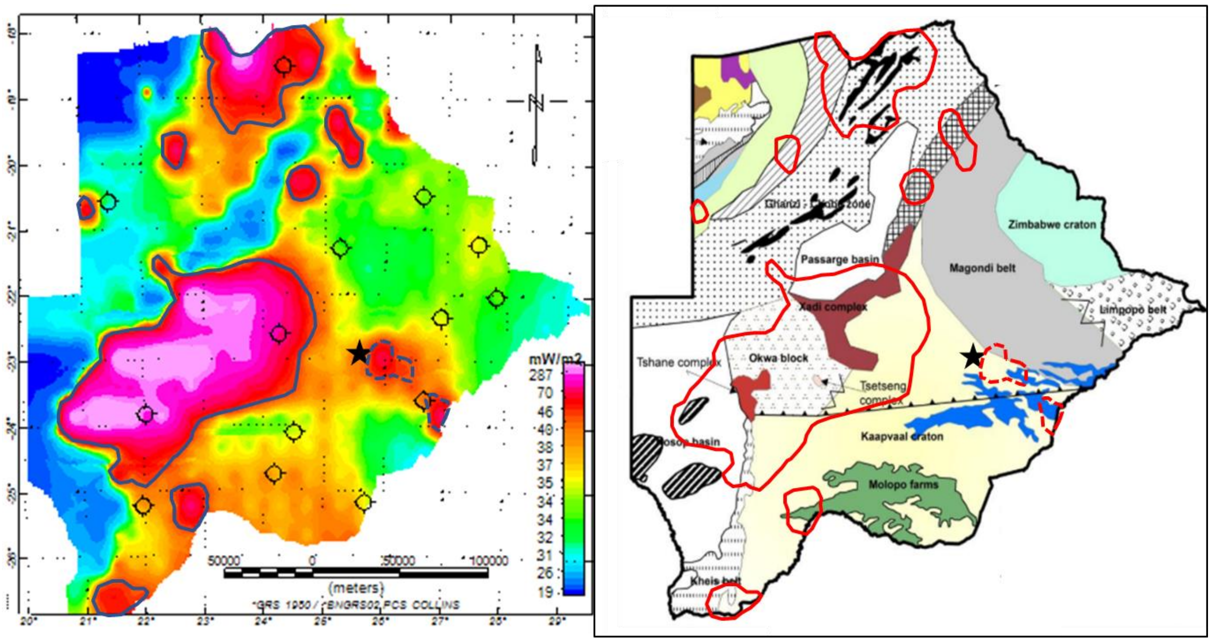

Figure 36 Geothermal prospect identification, the areas indicated by solid polygon are the area that has anomalous heat flow related to the continuation of EARS, the area highlighted by dashed polygon related to the older tectonic activity from the reactivation of Limpopo belt. (Left: heat flow map, right: geology map). The star indicates the epicentre of the 2017 earthquake in Botswana.

The first prospective zone is located along the extent of the Ghanzi-Chobe Belt in the northern part to Nosop Basin in the south-western part that interpreted as the continuation of the EARS in the study area. The lifted heat flow appeared in this area from the Okavango Rift Zone to the south-eastern part of Botswana. However, the actual value of the highest heat flow in these areas was not reliable due to the very shallow CPD. Geologically, the geothermal system that might be developed relatively the same with the south part of the western branch of EARS in Zambia and southern DR Congo. The rift from ORZ continued to the south-western Botswana that comprises of sedimentary basins.

The second prospective zone is situated in south-eastern Botswana. Despite having a relatively deeper CPD at around 20-25km, the anomalous heat flow was also found in these areas. The highest heat flow estimated in this area was 73 mW/m^2, this value is higher than the regional heat flow value for an Archean cratonic zone. According to Aldiss & Carney, (1992), there was a shear zone developed in this zone as the result of the reactivation of Limpopo Belt in Early Proterozoic era. This tectonic activity might be the reason behind the lifted heat flow in this area. Another possible explanation was, because of the earthquake that recently happened in this area. After all, an intensive study regarding the subsurface structure of this area is necessary to confirm the event that caused the anomalous high flow found in this area.

The high heat flow value (>65 mW/m^2) from other developed geothermal fields in the western branch of EARS were found in both geothermal prospect zones identified by this research. The more detailed study in this area is important to follow up the anomalous heat flow distinguished by this study. Further geothermal manifestation investigation in this area is required to get the information in the surface.

6. CONCLUSION AND RECOMMENDATION

6.1. Conclusion

This research has presented the Curie point depth and heat flow map for entire Botswana using aeromagnetic data. The maps were produced using the spectral analysis method (1D power spectral density) developed by Bouligand et al., (2009). The previously available geology and geophysical information were used for the comparison and validation of the results. The interpretation of the results provides the supporting evidence for the crustal thinning theory that proposed the continuation of EARS and defined the prospective geothermal areas for further exploration in Botswana.

The 1DPSD method used very much depended in several parameters, this problem was solved by executing the *pycurious* algorithm to search the parameter required in the power spectrum density equation (C, β, zt and Δz). Several assessments were performed in selecting the discrete wavenumber and window size for the algorithm requirements. The prior constraint of the depth was added from the crustal thickness model by Fadel, (2018). This study was able to estimate the variation of CPD value in entire Botswana. However, the result was giving a very shallow CPD (<1 km) which is not realistic to appear in this area. For this reason, the depth of the shallowest CPD was referred to the previous study in ORZ. The impact of this issue was also influencing the heat flow calculated in the study area. The highest heat flow estimated in these areas were above 200mW/m^2. The spatial distribution of the shallow CPD occurred within the thinner crust from the Okavango Rift Zone in the northeast to the south-western part of Botswana. Based on the comparison with the geological setting of the study area, the shallow CPD in the study area could also be the supporting evidence of the theory that proposes the continuation of East African Rift System in the study area. Several geothermal prospect zones were identified based on the anomalous heat flow and the geological condition of the study area.

This research has been able to answer the research questions as indicated below:

1. **Which area has shallow CPD? What is the value of the shallowest CPD?**
   The shallow CPD appears in the Okavango Rift Zone continuously to the south-western part of the study area following the extent of Ghanzi-Chobe Belt and in the sedimentary basins. The method used in this study was not able to estimate the realistic value of the shallowest CPD in Botswana, this is due to the limitation of the method that tends to overestimate the shallow CPD. However, the shallowest CPD estimated in the northern part of the study area are relatively comparable with the result from the previous study of 6-15km.
2. **How is the spatial relationship between the shallow CPD area and the observed crustal thinning in the study area?**
   The spatial distribution of the shallow CPD appears to be consistent with the observed crustal thinning in the study area. The area that has a thinner crust (<40km) is represented by the shallower CPD (<30km). Apart from the very shallow CPD, the value differences between CPD and crustal thickness is approximately around 10-15km. We hypothesize that the thinning crust initiates the lifted CPD, this is also supported by the geological condition of these areas.
3. **How is the heat flow value of the study area compared to the value of the developed geothermal field in the EARS? What is the effect of the different basement geology on the heat flow value?**
   This research was able to find the comparable heat flow value with the developed geothermal field in the EARS. There is a zone with the high flow higher than 82 mW/m^2 that comparable to the heat flow

around Lake Kivu (82±78 mW/m^2), Lake Tanganyika (65±36 mW/m^2) and Lake Malawi (67±46 mW/m^2). The basement geology explains that these areas are distributed in Ghanzi-Chobe Belt and the sedimentary basins from northern to southwestern of Botswana, and also in the south-eastern Botswana that is related to the Mahalapye complex, which all of them interpreted as the geologically weak zones.

4. **What is the implication of the crustal thinning theory to the geothermal prospect of the study area?**
   The thinner crust (<40km) influences the CPD to be shallower with the heat flow estimated in this area is relatively high. The identification of the geothermal prospect zones was based on the anomalous heat flow, these zones consequently to appear in the thinner crust. Furthermore, this geothermal identification was also supported by the geological condition of these areas. The areas that indicated as prospective areas were distributed in the continuation of EARS and the reactivated tectonic zone in south-western of Botswana.

6.2. Recommendation

This research was able to identify the geothermal prospect area based on the CPD and heat flow map on a regional scale. The following recommendations are:

1. A more detailed study in the central and southern part of Botswana is necessary, 3-D inversion method could be applied to overcome the limitation of the 1DPSD method in dealing with the very shallow CPD.
2. A study to review the extent of Congo Craton could be executed, this can help to explain the very deep CPD that was found in this research.
3. Further study the relationship between the high heat flow and the recent earthquake in south-eastern Botswana.
4. The surface geothermal investigation can be initiated to confirm the geothermal prospect of the study area, especially in ORZ while already studied by several studies.

LIST OF REFERENCES

Aboud, E., Alotaibi, A. M., & Saud, R. (2016). Relationship between Curie isotherm surface and Moho discontinuity in the Arabian shield, Saudi Arabia. *Journal of Asian Earth Sciences*, *128*, 42–53. https://doi.org/10.1016/J.JSEAES.2016.07.025

Aldiss, D. T., & Carney, J. N. (1992). The geology and regional correlation of the Proterozoic Okwa Inlier, western Botswana - PDF Free Download. *Precambrian Research*, *56*, 255–274.

Ballard, S., Pollack, H. N., & Skinner, N. J. (1987). Terrestrial heat flow in Botswana and Namibia. *Journal of Geophysical Research*, *92*(B7), 6291. https://doi.org/10.1029/JB092iB07p06291

Bertani, R. (2017). Introduction. In *Perspectives for Geothermal Energy in Europe* (pp. 1–9). WORLD SCIENTIFIC (EUROPE). https://doi.org/10.1142/9781786342324_0001

Bouligand, C., Glen, J. M. G., & Blakely, R. J. (2009). Mapping Curie temperature depth in the western United States with a fractal model for crustal magnetization. *Journal of Geophysical Research: Solid Earth*, *114*(B11). https://doi.org/10.1029/2009JB006494

Braun, J. (2009). Hot blanket in Earth's deep crust. *Nature*, *458*(7236), 292–293. https://doi.org/10.1038/458292a

Cermak, V., & Rybach, L. (1982). Thermal Properties. In G. Angenheister (Ed.), *Zahlenwerte und Funktionen ausNaturwissenschaft und Technik: Neue Serie* (New series, pp. 310–314). Berlin: Springer. Retrieved from https://www.researchgate.net/profile/Vladimir_Cermak/publication/258769285_Thermal_Conductivity_and_Specific_Heat_of_Minerals_and_Rocks/links/56d859b908aebe4638b6d082/Thermal-Conductivity-and-Specific-Heat-of-Minerals-and-Rocks.pdf

Chapman, D. S., & Pollack, H. N. (1977). Heat flow and heat production in Zambia: Evidence for lithospheric thinning in central Africa. *Tectonophysics*, *41*(1–3), 79–100. https://doi.org/10.1016/0040-1951(77)90181-0

Chisenga, C. (2015). *Understanding the earth structure underneath Botswana: The tectonic model and its relationship to the basement and crustal thickness (MSc Thesis)*. Enschede, Faculty of Geo-information Science and Earth Observation (ITC), University of Twente. Retrieved from https://webapps.itc.utwente.nl/librarywww/papers_2015/msc/aes/chisenga.pdf

Chopping, R., & Kennett, B. L. N. (2015). Maximum depth of magnetisation of Australia, its uncertainty, and implications for Curie depth. *GeoResJ*, *7*, 70–77. https://doi.org/10.1016/J.GRJ.2015.06.003

de Beer, J. H., V van Zijl, J. S., J Huyssen, R. M., V Hugo, P. L., Joubert, S. J., & Meyer, R. (1976). *A Magnetometer Array Study in South-West Africa, Botswana and Rhodesia* (Vol. 45). https://doi.org/10.1111/j.1365-246X.1976.tb00310.x

Eppelbaum, L., Kutasov, I., & Pilchin, A. (2014). *Applied Geothermics*. Berlin, Heidelberg: Springer Berlin Heidelberg. https://doi.org/10.1007/978-3-642-34023-9

Fadaie, K., & Ranalli, G. (1990). *Rheology of the lithosphere in the East African Rift System*. *Geophys. 1. Int* (Vol. 102). Retrieved from https://academic.oup.com/gji/article-abstract/102/2/445/656477

Fadel, I. (2018). *Crustal and upper mantle structure of Botswana: is Botswana rifting? (PhD Thesis)*. Enschede, Faculty of Geo-information Science and Earth Observation (ITC), University of Twente. Retrieved from https://webapps.itc.utwente.nl/librarywww/papers_2018/phd/fadel.pdf

Hardarson, B. S. (2016). *The western branch of the East African Rift: A review of tectonics, volcanology and geothermal* *activity*. Reykjavik. Retrieved from https://rafhladan.is/bitstream/handle/10802/13901/UNU-GTP-SC-23-0206.pdf?sequence=1

Hochstein, M. P. (1999). *Geothermal systems along the East-African Rift. Bulletin d'Hydrogiologie No* (Vol. 17). Retrieved from https://www.geothermal-energy.org/pdf/IGAstandard/EGC/1999/Hochstein.pdf

Key, R. M., & Ayres, N. (2000). The 1998 edition of the National Geological Map of Botswana. *Journal of African Earth Sciences*, *30*(3), 427–451. https://doi.org/https://www.sciencedirect.com/science/article/pii/S0899536200000300

Khoza, D., Jones, A. G., Muller, M. R., Evans, R. L., Miensopust, M. P., & Webb, S. J. (2013). Lithospheric structure of an Archean craton and adjacent mobile belt revealed from 2-D and 3-d inversion of magnetotelluric data: Example from southern Congo craton in northern Namibia. *J. Geophys. Res. Solid Earth*, *118*, 4378–4397. https://doi.org/10.1002/jgrb.50258

Kinabo, B. D., Atekwana, E. A., Hogan, J. P., Modisi, M. P., Wheaton, D. D., & Kampunzu, A. B. (2007). Early structural development of the Okavango rift zone, NW Botswana. *Journal of African Earth Sciences*, *48*(2–3), 125–136. https://doi.org/10.1016/J.JAFREARSCI.2007.02.005

King, D., Metcalfe, E., Fellow, T. P., Office, G. T., & Office, T. (2013). Rift zones as a case study for advancing geothermal occurrence models. *Proceedings of the 38th Workshop on Geothermal Reservoir Engineering, Stanford, CA*. Retrieved from http://geothermaldata.org/

Leseane, K., Atekwana, E. A., Mickus, K. L., Abdelsalam, M. G., Shemang, E. M., & Atekwana, E. A. (2015). Thermal perturbations beneath the incipient Okavango Rift Zone, northwest Botswana. *Journal of Geophysical Research*, *120*, 1210–1228. https://doi.org/10.1002/2014JB011029

Li, C.-F., Shi, X., Zhou, Z., Li, J., Geng, J., & Chen, B. (2010). Depths to the magnetic layer bottom in the South China Sea area and their tectonic implications. *Geophysical Journal International*, *182*(3), 1229–1247. https://doi.org/10.1111/j.1365-246X.2010.04702.x

Limberger, J., Boxem, T., Pluymaekers, M., Bruhn, D., Manzella, A., Calcagno, P., … van Wees, J.-D. (2018). Geothermal energy in deep aquifers: A global assessment of the resource base for direct heat utilization. *Renewable and Sustainable Energy Reviews*, *82*, 961–975. https://doi.org/10.1016/j.rser.2017.09.084

Maus, S., Gordon, D., & Fairhead, D. (1997). Curie-temperature depth estimation using a self-similar magnetization model. *Geophysical Journal International*, *129*(1), 163–168. https://doi.org/10.1111/j.1365-246X.1997.tb00945.x

Midzi, V., Saunders, I., Manzunzu, B., Kwadiba, M. T., Jele, V., Mantsha, R., … Zulu, B. S. (2018). The 03 April 2017 Botswana M6.5 earthquake: Preliminary results. *Journal of African Earth Sciences*, *143*, 187–194. https://doi.org/10.1016/J.JAFREARSCI.2018.03.027

Mielke, P., Bär, K., & Sass, I. (2017). Determining the relationship of thermal conductivity and compressional wave velocity of common rock types as a basis for reservoir characterization. *Journal of Applied Geophysics*, *140*(April), 135–144. https://doi.org/10.1016/j.jappgeo.2017.04.002

Okubo, Y., Graf, R. J., Hansen, R. O., Ogawa, K., & Tsu, H. (1985). Curie point depths of the Island of Kyushu and surrounding areas, Japan. *GEOPHYSICS*, *50*(3), 481–494. https://doi.org/10.1190/1.1441926

Omenda, P. A. (2013). *The geothermal activity of the East African Rift*. Naivasha. Retrieved from https://orkustofnun.is/gogn/unu-gtp-sc/UNU-GTP-SC-05-34b.pdf

Richter. (2011). Kalahari Energy enters MOU on geothermal exploration rights in Zambia | Think GeoEnergy - Geothermal Energy News. Retrieved July 31, 2018, from http://www.thinkgeoenergy.com/kalahari-energy-enters-mou-on-geothermal-exploration-rights-in-zambia/

Robertson, E. C. (1988). Thermal properties of rocks. Report 88-441. *US Department of the Interior: Geological Survey*, 106. https://doi.org/10.3133/ofr88441

Rojas, F. (2015). The UNEP/ GEF African Rift Geothermal Development Facility (ARGeo) | Think GeoEnergy - Geothermal Energy News. Retrieved August 4, 2018, from http://www.thinkgeoenergy.com/the-unep-gef-african-rift-geothermal-development-facility-argeo/

Singletary, S. J., Hanson, R. E., Martin, M. W., Crowley, J. L., Bowring, S. A., Key, R. M., … Krol, M. A. (2003). Geochronology of basement rocks in the Kalahari Desert, Botswana, and implications for regional Proterozoic tectonics. *Precambrian Research*, *121*(1–2), 47–71. https://doi.org/10.1016/S0301-9268(02)00201-2

Spector, A., & Grant, F. S. (2002). Statistical models for interpreting aeromagnetic data. *Geophysics*, *35*(2), 293–302. https://doi.org/10.1190/1.1440092

Stein, C. A. (1995). Heat Flow of the Earth. In *Global Earth Physics - A handbook of physical constants* (pp. 144–158). Washington DC: American Geophysical Union. Retrieved from http://www.unicamp.br/fea/ortega/extensao/Stein.pdf

Tanaka, A., Okubo, Y., & Matsubayashi, O. (1999). Curie point depth based on spectrum analysis of the magnetic anomaly data in East and Southeast Asia. *Tectonophysics*, *306*(3–4), 461–470. https://doi.org/10.1016/S0040-1951(99)00072-4

APPENDICES

Appendix 1: The location of the wells

The image shows the distribution of the wellbore across Botswana and Namibia, 14 of 25 wells located in Botswana were used in this research.

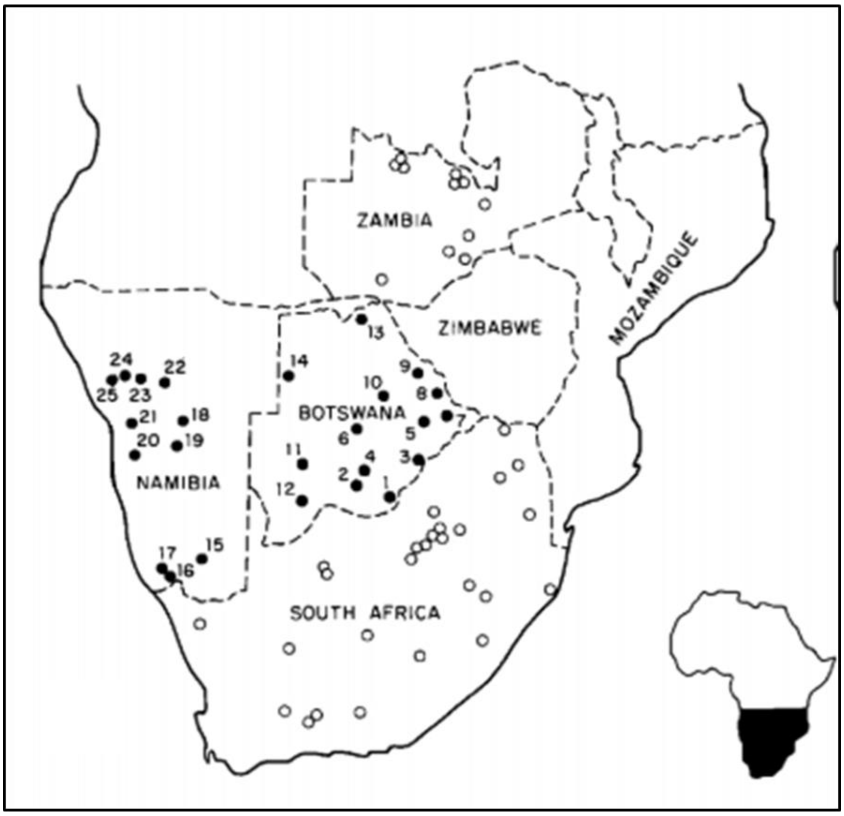

Appendix 2: Thermal conductivity of various rocks (Cermak & Rybach, 1982)

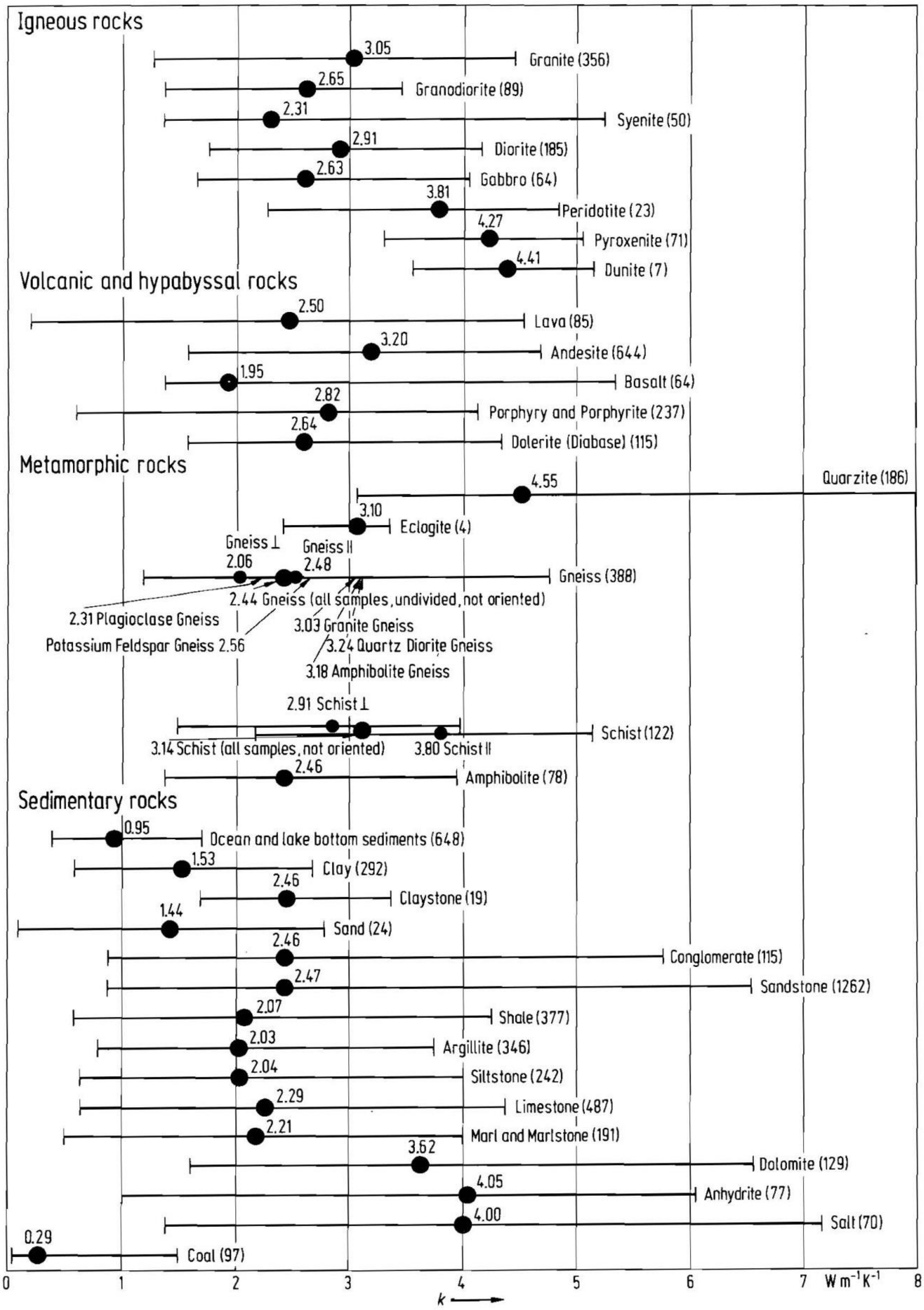

Appendix 3: The relationship between thermal conductivity and temperature changes (Robertson, 1988)

Temperature effect on thermal conductivity of several rocks (Robertson, 1988). (Left: sedimentary rocks, centre: ultramafic rocks and right: felsic rocks)

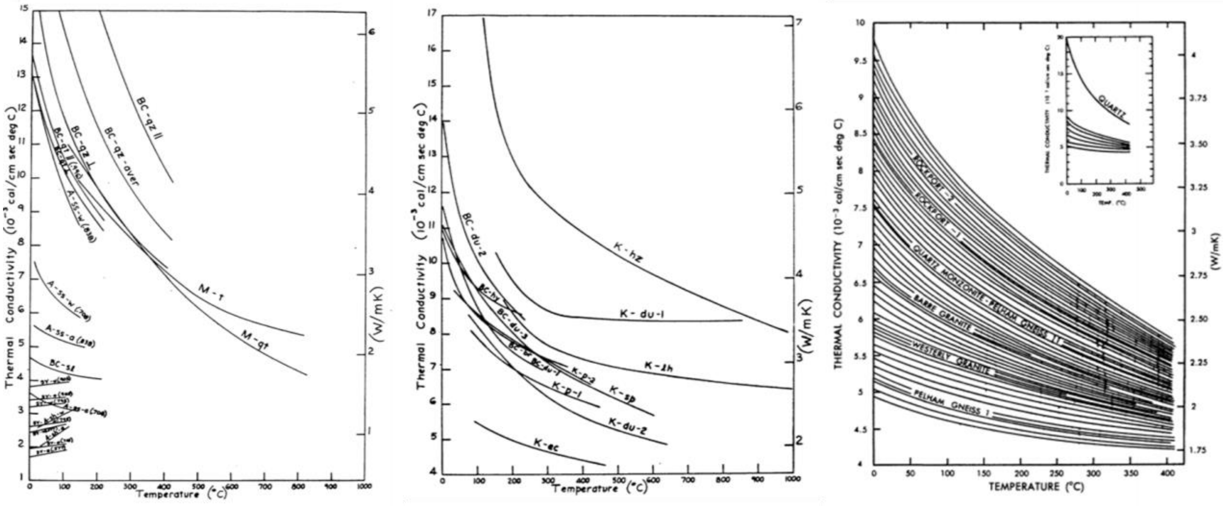

Appendix 4: CPD and uncertainty result unmasked.

The CPD and uncertainty result shown in Figure 17 were already masked to the border of Botswana. Here are the original maps produced by the *pycurious* algorithm. a & b). CPD and uncertainty of 200m pixel size. c & d). CPD and uncertainty of 400m pixel size. e & f). CPD and uncertainty of 800m pixel size.

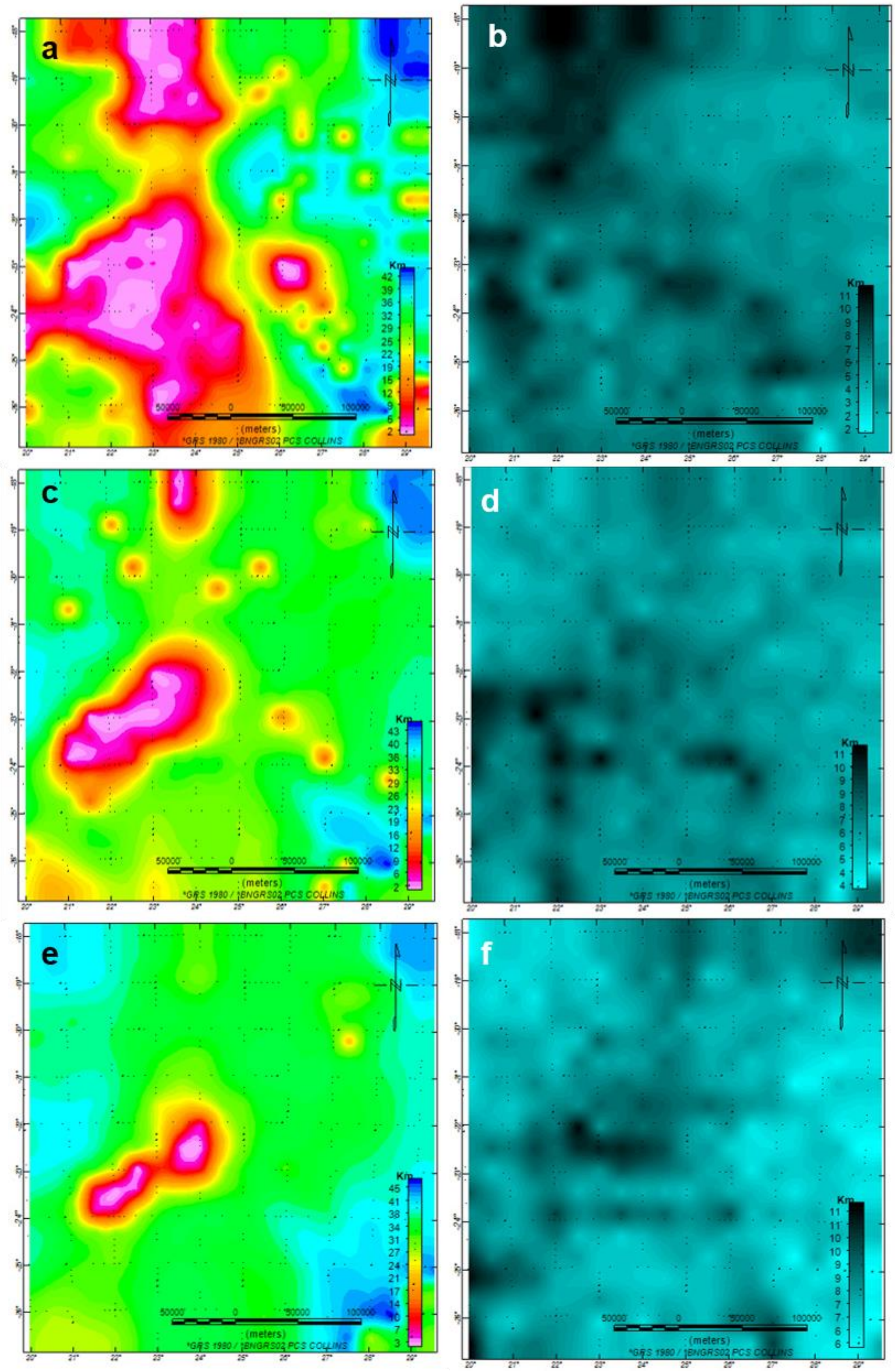

Appendix 5: Statistic of the magnetic data input of each window from the artefact and its surrounding.

The statistic of the window that creates artefact shown in number 3.

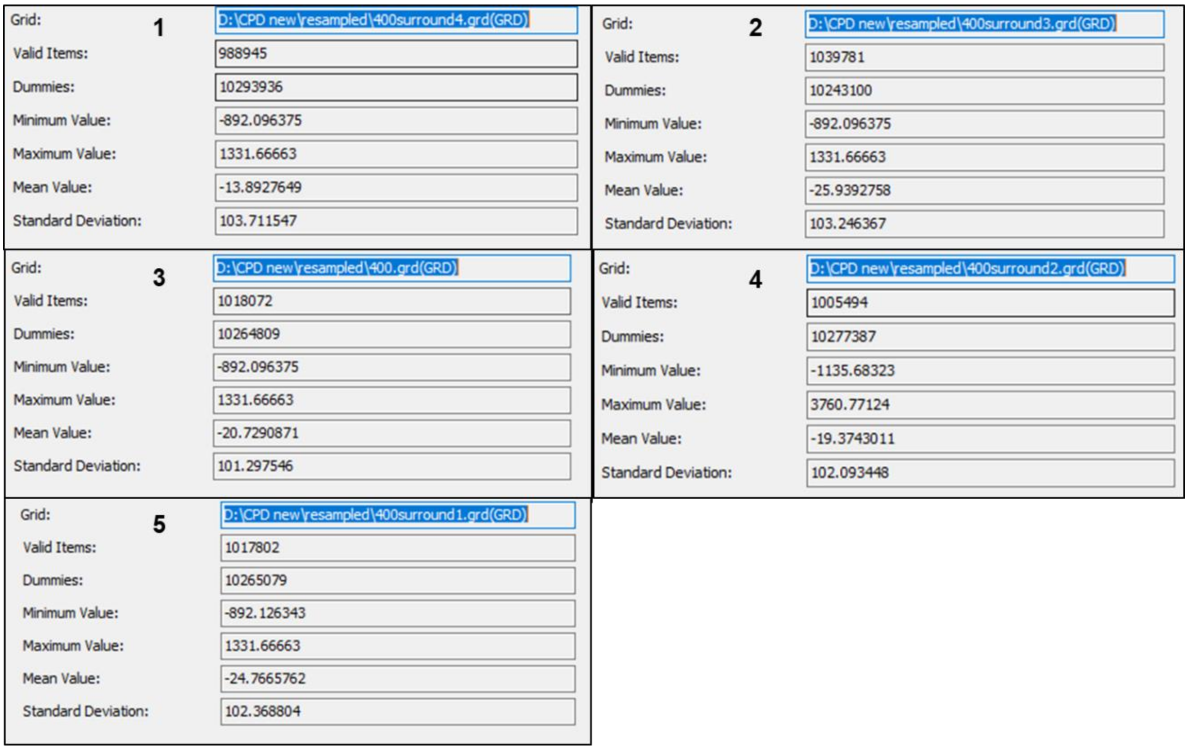

1

Grid: D:\CPD new\resampled\400surround4.grd(GRD)
Valid Items: 988945
Dummies: 10293936
Minimum Value: -892.096375
Maximum Value: 1331.66663
Mean Value: -13.8927649
Standard Deviation: 103.711547

2

Grid: D:\CPD new\resampled\400surround3.grd(GRD)
Valid Items: 1039781
Dummies: 10243100
Minimum Value: -892.096375
Maximum Value: 1331.66663
Mean Value: -25.9392758
Standard Deviation: 103.246367

3

Grid: D:\CPD new\resampled\400.grd(GRD)
Valid Items: 1018072
Dummies: 10264809
Minimum Value: -892.096375
Maximum Value: 1331.66663
Mean Value: -20.7290871
Standard Deviation: 101.297546

4

Grid: D:\CPD new\resampled\400surround2.grd(GRD)
Valid Items: 1005494
Dummies: 10277387
Minimum Value: -1135.68323
Maximum Value: 3760.77124
Mean Value: -19.3743011
Standard Deviation: 102.093448

5

Grid: D:\CPD new\resampled\400surround1.grd(GRD)
Valid Items: 1017802
Dummies: 10265079
Minimum Value: -892.126343
Maximum Value: 1331.66663
Mean Value: -24.7665762
Standard Deviation: 102.368804

Appendix 6: CPD results after shifting the centroid of 1DPSD vertically and horizontally

The CPD map after shifting the centroid of 1DPSD a) horizontally, b) vertically. The artefacts always appear in any results.

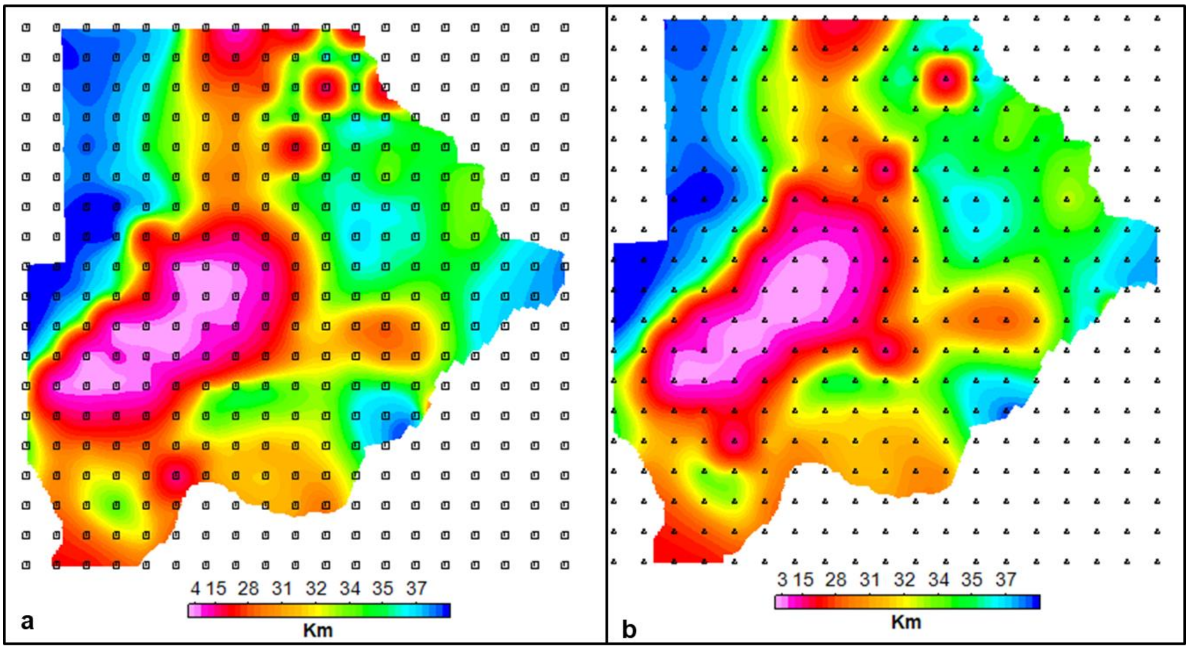

Appendix 7: Python code for CPD estimation using *pycurious* algorithm (modified).

A python module called *pycurious* was created by Dr. Ben Mather from the University of Sydney. The module was downloaded from https://github.com/brmather/pycurious

Here is the python code to calculate CPD using 1DPSD method by Bouligand et al., (2009) that was used in this study.

```
# import python modules
import numpy as np
import matplotlib.pyplot as plt
import openpyxl
from openpyxl import Workbook
from openpyxl import load_workbook
from scipy import stats
import pycurious

# load magnetic anomaly
mag_data=np.loadtxt("C:\\yourdirectory\\yourmagneticdata.txt")

#reshaping the magnetic data
x = mag_data[:,0]
y = mag_data[:,1]

xmin, xmax = x.min(), x.max()
ymin, ymax = y.min(), y.max()
print (xmax, xmin, ymin, ymax)

dx, dy = 400, 400 # grid resolution (pixel size)
nx, ny = int(round((xmax-xmin)/dx)+1), int(round((ymax-ymin)/dy)+1)

d = mag_data[:,2].reshape(ny,nx)

# filter NaNs value
mag_data = mag_data[mag_data[:,2] != 9999.]

grid = pycurious.CurieOptimise(d, xmin, xmax, ymin, ymax)

# define the centroid of the window
window_size = 400e3
xc_list, yc_list = grid.create_centroid_list(window_size,
spacingX=50e3, spacingY=50e3)

print("number of centroids = {}".format(len(xc_list)))

# get dimensions of domain
xcoords = np.unique(xc_list)
ycoords = np.unique(yc_list)
nc, nr = xcoords.size, ycoords.size
print (nc,nr)

# adding the prior constraint
```

```
grid.reset_priors()
grid.add_prior(dz=(40.0,10.0))

# calculating 1DPSD using bouligand
beta, zt, dz, C = grid.optimise_routine(window_size, xc_list,
yc_list)



# plot results
fig, (ax1, ax2, ax3, ax4) = plt.subplots(1, 4, sharex=True,
sharey=True, figsize=(17,3.))

im1 = ax1.imshow(beta.reshape(nr,nc))
im2 = ax2.imshow(zt.reshape(nr,nc))
im3 = ax3.imshow(dz.reshape(nr,nc))
im4 = ax4.imshow(C.reshape(nr,nc))

fig.colorbar(im1, ax=ax1, label=r"$\beta$")
fig.colorbar(im2, ax=ax2, label=r"$z_t$")
fig.colorbar(im3, ax=ax3, label=r"$\Delta z$")
fig.colorbar(im4, ax=ax4, label=r"$C$")

np.savetxt("beta.txt", beta, delimiter=" ")
np.savetxt("zt.txt", zt, delimiter=" ")
np.savetxt("dz.txt", dz, delimiter=" ")
np.savetxt("C.txt", C, delimiter=" ")

# plot Curie depth

#curie_depth = zt + dz

#fig = plt.figure()
#ax1 = fig.add_subplot(111)
#im1 = ax1.imshow(curie_depth.reshape(nr,nc), cmap=plt.cm.BrBG)
#fig.colorbar(im1)

#scale of each parameter search
x_scale = [0.25, 0.1, 1.0, 0.5]

# run simulations for production runs
burnin = 1000
nsim = 5000

# mean across the domain
mu_beta, mu_zt, mu_dz, mu_C = beta.mean(), zt.mean(), dz.mean(),
C.mean()

pt_post = []

# This will take some time
for xc, yc in zip(xc_list, yc_list):
    posterior = grid.metropolis_hastings(window_size, xc, yc, nsim,
burnin, x_scale,\
```

```
                                         mu_beta, mu_zt, mu_dz,
mu_C, taper=None)
    pt_post.append( posterior )

curie_depth = np.zeros_like(xc_list)
uncertainty = np.zeros_like(xc_list)

for i, pt in enumerate(pt_post):
    betaP, ztP, dzP, CP = pt
    cpd = ztP + dzP
    curie_depth[i] = np.mean(cpd)
    uncertainty[i] = np.std(cpd) #standard deviation of the result

#sensitivity

beta_p = stats.norm(3.0, 1.0)
grid.add_prior(beta=beta_p)

nsim = 100
pt_post = []

for xc, yc in zip(xc_list, yc_list):
    sensitivity = grid.sensitivity(window_size, xc, yc, nsim,
mu_beta, mu_zt, mu_dz, mu_C, taper=None)
    pt_post.append( sensitivity )

curie_depth = np.zeros_like(xc_list)
uncertainty = np.zeros_like(xc_list)

for i, pt in enumerate(pt_post):
    betaP, ztP, dzP, CP = pt
    cpd = ztP + dzP
    curie_depth[i] = np.mean(cpd)
    uncertainty[i] = np.std(cpd)

# plot Curie depth

curie_depth = zt + dz

fig, (ax1,ax2) = plt.subplots(1,2, figsize=(11,4))
im1 = ax1.imshow(curie_depth.reshape(nr,nc), cmap=plt.cm.BrBG)
im2 = ax2.imshow(uncertainty.reshape(nr,nc), cmap=plt.cm.Blues)
fig.colorbar(im1, ax=ax1)
fig.colorbar(im2, ax=ax2)
#print (curie_depth)
ax1.set_title("Curie depth (km)")
ax2.set_title("Uncertainty (km)")

np.savetxt("xcoord.txt", xc_list, delimiter=" ")
np.savetxt("ycoord.txt", yc_list, delimiter=" ")
np.savetxt("CPD.txt", curie_depth, delimiter=" ")
np.savetxt("uncertainty.txt", uncertainty, delimiter=" ")

#to import the result to excel sheets
def to_excel():
```

```
    path= 'C:\\youdirectory\\excelsheets.xlsx'
    wb=load_workbook(path)
    a=nc
    b=nr
    with open ('C:\\yourdirectory\\xcoord.txt', 'r+') as d:
        xcoords=d.readlines()
    with open ('C:\\ yourdirectory \\ycoord.txt', 'r+') as e:
        ycoords=e.readlines()
    with open ('C:\\ yourdirectory \\CPD.txt', 'r+') as f:
        cpd=f.readlines()
    with open ('C:\\ yourdirectory \\uncertainty.txt', 'r+') as g:
        uncertainty=g.readlines()
    z=1
    for z in range (1,b+1):
    #for z in range (1,4):
        ws=wb[('Sheet'+str(z))]
        #for row in range (1,42):
        for row in range (1,a+1):
            xcoor=ws.cell(row=row, column=1)
            xcoor.value=float(xcoords[0])
            del xcoords[0]
            ycoor=ws.cell(row=row, column=2)
            ycoor.value=float (ycoords[0])
            del ycoords[0]
            curie=ws.cell(row=row, column=3)
            curie.value=float (cpd[0])
            del cpd[0]
            uncer=ws.cell(row=row, column=4)
            uncer.value=float (uncertainty[0])
            del uncertainty[0]
        wb.create_sheet('Sheet'+str(z+1))
        spath=r'C:\yourdirectory\''
        final=spath+('yourfilename.xlsx')
        wb.save(final)

#import to excel and show the final image of the results
to_excel()
plt.show()
```